

## Article

# Robust, Model-Based External Calibration of Multi-Channel Airborne SAR Sensors Using Range Compressed Raw Data

Marc Jäger , Rolf Scheiber  and Andreas Reigber 

Microwaves and Radar Institute, German Aerospace Center (DLR), Münchener Str. 20, 82234 Weßling, Germany; rolf.scheiber@dlr.de (R.S.); andreas.reigber@dlr.de (A.R.)

\* Correspondence: marc.jaeger@dlr.de; Tel.: +49-815328-2802

Received: 28 September 2019; Accepted: 12 November 2019; Published: 15 November 2019



**Abstract:** The paper describes a method for the accurate calibration of multi-channel SAR instruments, such as those required to support SAR polarimetry, single-pass interferometry and digital beam-forming (DBF), on the basis of dedicated SAR acquisitions containing reference targets with known properties. Unlike conventional approaches, the method is based entirely on the analysis of range-compressed raw data. It leverages the pulse-by-pulse analysis of amplitude, phase and delay variations observed within the range histories of reference targets to fully characterize and correct propagation direction dependent calibration issues such as those related to antenna pointing or antenna phase center positions. The fact that the approach does not require SAR image focusing in azimuth is especially relevant in the context of DBF, where individual channels need to be calibrated but are, by themselves, under-sampled. The calibration techniques presented are illustrated and validated using multi-channel polarimetric and single-pass interferometric SAR data acquired by DLR's airborne F-SAR and DBFSAR instruments.

**Keywords:** Synthetic Aperture Radar; external calibration; SAR polarimetry; SAR interferometry; digital beam-forming; baseline calibration; geometric calibration; antenna pointing

## 1. Introduction

Synthetic Aperture Radar (SAR) imaging aims to characterize the interaction of the transmitted electromagnetic waves with scatterers in the imaged scene. In practice, the recorded SAR raw data do describe these interactions but also include a multitude of effects that are due to the SAR sensor hardware and the propagation of signals within it. These systematic, sensor induced effects are not related to the contents of the imaged scene and hinder a meaningful interpretation of the resulting imagery. Such issues are especially relevant in the case of advanced SAR sensors, with analog or even digital beam-forming (DBF), that employ antenna arrays: systematic errors at the level of the individual antenna array element will impair or even prohibit image formation itself, as the effective antenna illumination patterns will deviate from the expectation and lead to errors in SAR focusing.

The continued interest in scientific and operational exploitation of SAR in a diverse set of remote sensing applications has lead to ever more stringent requirements regarding the calibration quality of SAR data delivered by modern sensors. At the same time, SAR sensors are becoming more complex and consequently more difficult to calibrate. This is especially true for new SAR imaging modes that involve simultaneous data acquisition in multiple channels for polarimetric imaging, single-pass interferometry or DBF. The task of SAR sensor calibration is therefore becoming simultaneously more important from an application point of view and more difficult in view of the underlying sensor complexity.

This is especially true for airborne SAR sensors for research, which play an important role in the process of SAR sensor development and are often technological precursors of the next generation of satellite SAR sensors. The DLR's Microwaves and Radar Institute currently operates several airborne SAR sensors that cover a wide range of innovative imaging techniques, including polarimetric imaging, single-pass polarimetric multi-baseline interferometry and multi-channel along-track interferometry. This paper details a general calibration approach that was developed to meet the diverse requirements implied by these multi-channel SAR imaging modes. As such, the approach necessarily entails multiple steps that address calibration issues related to imaging geometry, radiometry and the polarimetric/interferometric inter-channel phase difference.

SAR sensor calibration generally involves both internal calibration and external calibration [1]. Internal calibration is based on measurements performed internally by the SAR sensor. These can later be used to correct for distortions and transient drifts when radar pulses are transmitted or received.

The discussion in this paper takes the internal calibration as a given and is mainly concerned with aspects of SAR sensor calibration that are outside the scope of internal measurements. These aspects make up the external sensor calibration, in which actual SAR measurements of reference targets with known properties are analyzed to refine an existing sensor model. These refinements are primarily concerned with the multi-aperture antenna array of the multi-channel SAR sensor under consideration.

The relevant properties of reference targets, such as position, size and orientation, among others, must be well known such that the targets' expected radar return can be predicted with a high degree of accuracy for any given imaging geometry. External sensor calibration is then the process of estimating corrections to eliminate systematic deviations of the measured target response from the a priori expectation.

The calibration technique discussed in this paper differs from existing techniques in that it is based entirely on range compressed raw data, instead of relying on the analysis of focused SAR imagery. The novelty lies in analyzing the response of reference targets in a pulse-by-pulse fashion, such that additional information concerning the variation of key quantities within the illumination time of each target can be leveraged in the estimation of propagation direction dependent calibration corrections.

As will be argued in the next section, this approach is especially suited in the context of multi-channel SAR and DBF. A more general advantage of basing the calibration directly on raw data, rather than focused imagery, is that it ensures independence from the SAR processor. Modern SAR processors are highly complex and it is often difficult to distinguish calibration issues that arise at the sensor level from errors introduced by the processor in focusing the SAR imagery. Decoupling the processor from the task of calibration reduces complexity and can help pinpoint issues in the SAR processor. Calibration results do not transfer to the focused SAR imagery as expected in the presence of processing artifacts.

The remainder of the paper is organized as follows: Section 2 provides an overview of the state of the art in external SAR sensor calibration and indicates the contributions of the proposed approach. Section 3 introduces the reference target response model used and describes how the SAR data in calibration acquisitions are analyzed to quantify any mismatch between the measured and the expected target response. Section 4 describes how a rigorous optimization process connects the measured response mismatch to appropriate calibration corrections, while Section 5 illustrates and validates the approach using real multi-channel SAR data and finally Section 6 concludes the paper.

## 2. State of the Art

A number of recent satellite SAR missions have involved extensive, well-documented and highly successful external calibration programs. Representative examples include the approaches developed for the TerraSAR-X [2] and TanDEM-X [3] missions, launched in 2007 and 2010, respectively, as well as the Cosmo-Skymed mission [4], with four satellites launched between 2007 and 2010, the Sentinel-1 mission [5], with satellites A and B launched in 2014 and 2016, respectively, and the Radarsat-2

mission [6]. Similar techniques have also been applied for the calibration of airborne SAR sensors, such as the F-SAR sensor operated by the German Aerospace Center (DLR) [7,8].

All of the above satellite missions feature highly complex radar instruments with phased-array antennas consisting of hundreds of individually controlled antenna elements to support advanced SAR imaging modes. Different imaging modes are facilitated by beam-forming techniques that combine signals from multiple antenna elements within the instrument. Here, amplitude and phase adjustments to individual signals change the effective antenna diagram while data are being acquired.

This type of SAR sensor represents a considerable challenge in terms of calibration due to the large configuration space required to support a variety of imaging modes. In the case of the TerraSAR-X and TanDEM-X sensors, for instance, the operational imaging modes are defined in terms of more than 10,000 unique effective antenna patterns [9] (also known as ‘beams’). Due to limited resources, in terms of time during the sensor commissioning phase and budget, it is neither possible nor desirable to attempt the individual characterization and calibration of these beams on the basis of SAR measurements acquired after the sensor has been deployed in orbit. Instead, large parts of the calibration effort are based on an antenna model [9,10] that is able to accurately reproduce the effective antenna illumination pattern given the settings applied at the level of the individual antenna array element. This model can then be validated by comparing its predictions with actual SAR measurements for a comparatively tiny number of beams. Once validated, it is assumed to generalize to all other beams employed during operational data acquisition and may be relied upon to provide the detailed, propagation direction dependent antenna characterization that is used to compensate for systematic antenna-related effects during SAR data processing.

A major focus of external calibration activities in the context of modern SAR missions is therefore the validation of the antenna model. Studies [9] and [11] outline the external validation of the antenna models used for the TerraSAR-X and Sentinel-1A SAR instruments, respectively. Similar calibration approaches have been used for the COSMO-SkyMed [12] and Radarsat-2 [13] instruments. These approaches are similar and comprise a set of techniques to assess the antenna diagrams in elevation and azimuth and estimate the antenna mispointing. Focused SAR imagery acquired over areas of homogeneous backscatters, typically the Amazon rain forest, are used to validate the elevation antenna diagram and estimate the elevation mispointing. The later estimate uses dedicated acquisitions employing a *notch* antenna pattern. In azimuth, meanwhile, the validation of the diagram and the mispointing estimate are based on active calibration targets [14]. For polarimetric sensors, acquisitions with active targets can also be used for polarimetric cross-talk calibration [15].

In addition to antenna model validation, external calibration also entails the estimation calibration constants that account for constant offsets in gain, delay and phase that are mainly due to propagation effects within the instrument. These constants are estimated using reference targets with known properties, such that their expected response in SAR acquisitions can be predicted accurately. The analysis of reference target returns is carried out in focused SAR imagery of point-like targets [1,16], such as radar reflectors or specifically selected distributed targets, such as water surfaces [17].

Notwithstanding the success and proven accuracy of established calibration techniques, the approach presented in the following sections may offer certain advantages in the context of multi-channel SAR systems. Firstly, conventional external calibration techniques rely heavily on focused SAR imagery. In addition to the arguably undesirable reliance on SAR processing software, the use of focused imagery may not even be an option for multi-channel systems that require analog or digital beam-forming techniques, in range or in azimuth, carried out on board or on ground, for image formation. For such instruments, image formation supposes a well-calibrated antenna array but calibration requires image formation. The present approach circumvents this circular problem, as it does not require SAR image formation and can be applied to data that are under-sampled in azimuth. Similarly, it can be applied without modification in arbitrary imaging geometries, such as circular SAR [18], or to data that is irregularly sampled in azimuth [19].

Secondly, existing approaches are geared towards verifying an existing antenna model. They do not, generally, include mechanisms to systematically work backwards from an observed mismatch between expectation and observation to a set of causes for the mismatch and the corresponding corrections. The proposed approach introduces explicit error models and derives corrections through a rigorous optimization process. In particular, it explicitly addresses uncertainty in the three dimensional antenna phase center positions to ensure the consistent inter-channel phase and geometry that are of central importance in most multi-channel SAR applications. Furthermore, the optimization approach naturally lends itself to a more detailed modeling of error sources. For instance, the proposed antenna mispointing estimate can derive three dimensional roll/pitch/yaw corrections, rather than the conventional elevation/azimuth estimates. It can also provide separate corrections for the transmit and receive channels when these involve different antennas.

### 3. Target Response Model and Analysis

As outlined in Figure 1, the proposed external calibration workflow starts with the analysis of reference target responses in multiple channels of acquired SAR data. The analysis is repeated throughout the calibration process to take into account each calibration correction as it becomes available.

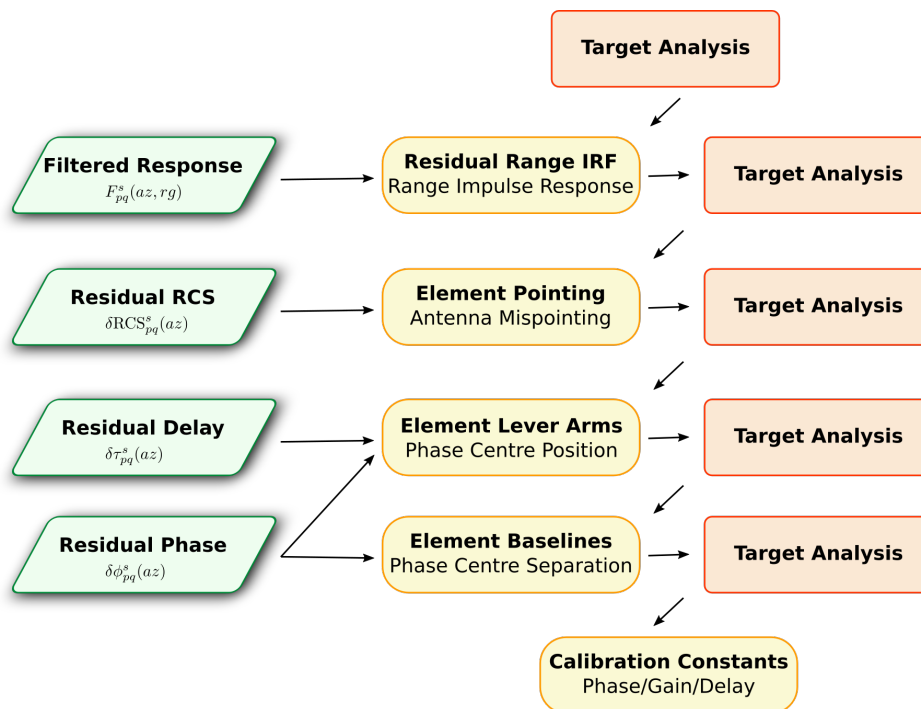


**Figure 1.** A flowchart illustrating the calibration process. The columns, from right to left, correspond to the target analysis of Section 3.2, the estimation of individual calibration corrections described in Section 4 and the inputs used by estimation step (derived from the previous iteration of analysis).

The notation adopted throughout the following sections uses  $az$  to denote the azimuth sample index and super- and sub-scripts  $\square_{pq}^s$  to indicate any quantity derived from the response of reference target  $s$  in a SAR data channel that uses the antenna elements  $p$  and  $q$  on transmit and receive, respectively. An antenna element is, for the present purposes, the smallest constituent of an antenna array that can individually send and/or receive signals. In particular, polarimetric antennas are considered as two independent elements corresponding to the horizontal and vertical polarizations.

The calibration approach is intended to be applied to a data set comprising one or more calibration data acquisitions. Such acquisitions contain reference targets that are imaged over a wide range of off-nadir angles. To avoid unnecessary complication of the notations adopted, the reference target



superscript  $s$  is specific to the data acquisition. Thus, when the same target appears in independent acquisitions, the responses are treated as though originating from different targets.

### 3.1. Acquisition Geometry and Response Model

External calibration entails the comparison of the measured target response with the expectation. The expected response depends on sensor and target properties, but also on the acquisition geometry. For the purposes of calibration, it is convenient to describe the geometry in a rest frame of the instrument. This frame is a Cartesian coordinate system that translates and rotates with the sensor platform. A fixed point  $\vec{x}_{global}$  in a global coordinate system transforms into a time-variant coordinate  $\vec{x}_{instr}(t)$  in the instrument coordinate system as

$$\vec{x}_{instr}(t) = \mathbf{R}_{G \rightarrow I}(t) \left( \vec{x}_{global} - \vec{N}(t) \right), \quad (1)$$

where  $\vec{N}(t)$  is the position of the instrument reference point in global coordinates, as measured by the navigation subsystem, and  $\mathbf{R}_{G \rightarrow I}(t)$  denotes the rotation into the rest frame and depends on the time variant sensor attitude angles.

In instrument coordinates, the phase centre of an antenna element  $e \in \{p, q\}$  is constant and is given by the sum of  $\vec{L}_e$  and  $\Delta\vec{L}_e$ . These former represents the assumed phase center position. The latter denotes the correction to this position introduced in the process of sensor calibration. It is initially assumed to be zero.

The position of the target  $\vec{T}^s(t)$  is obtained from the known global target coordinate via the transform (1). The position of the target relative to a phase centre  $e$  is then defined as

$$\vec{r}_e^s(az) = \vec{T}^s(t_{pq}(az)) - \left( \vec{L}_e + \Delta\vec{L}_e \right), \quad (2)$$

where  $t_{pq}(az)$  is the channel dependent mapping from azimuth sample index  $az$  onto the continuous time axis  $t$ . Note that this formulation assumes that the *start-stop* effect can be ignored, as is the case for airborne SAR but not for spaceborne platforms and high spatial resolutions [20].

Normalizing the relative position of the target gives the azimuth variant line of sight (LOS) vectors towards the target:

$$\vec{los}_e^s(az) = \frac{\vec{r}_e^s(az)}{|\vec{r}_e^s(az)|} \quad (3)$$

In a given acquisition geometry, the expected target response  $M_{pq}^s(az, f_r)$  varies as a function of the azimuth sample index  $az$  and the physical range frequency  $f_r$ . This response has an amplitude that is closely related to the radar equation for real aperture radar [21] as well as a phase related to the spatial separation of sensor and target. The combination of these terms is the response model underlying the calibration process:

$$M_{pq}^s(az, f_r) = \frac{c A_{pq}^s(az, f_r)}{\sqrt{4\pi} f_r} \frac{R_{pq}^s(az, f_r)}{4\pi \prod_{e \in \{p, q\}} |\vec{r}_e^s(az)|} e^{j\phi_{pq}^s(az, f_r)}, \quad (4)$$

where  $c$  is the speed of light and  $j$  denotes  $\sqrt{-1}$ .

The phase of the reference target response is related to the target range and can be written as

$$\phi_{pq}^s(az, f_r) = -2\pi \frac{f_r}{(1 + \Delta c) c} \sum_{e \in \{p, q\}} |\vec{r}_e^s(az)|, \quad (5)$$

where  $\Delta c$  is a tropospheric propagation delay correction that is introduced in the calibration process and is initially assumed zero.

The power of the response, meanwhile, is given by the received signal power as defined in the context of the radar equation for real aperture radar [21]. It includes the free space propagation loss in the denominator as well as the azimuth variant antenna amplification  $A_{pq}^s(az, f_r)$  and the target backscatter amplitude  $R_{pq}^s(az, f_r)$ . The antenna amplification is given by

$$A_{pq}^s(az, f_r) = \prod_{e \in \{p, q\}} A_e\left(\alpha\left(\mathbf{R}_{I \rightarrow e} \vec{\mathbf{los}}_e^s(az)\right), \beta\left(\mathbf{R}_{I \rightarrow e} \vec{\mathbf{los}}_e^s(az)\right), f_r\right), \quad (6)$$

where  $A_e(\alpha, \beta, f_r)$  is the complex valued antenna diagram of element  $e$ , which is a function of propagation direction (angles  $\alpha$  and  $\beta$ ) and frequency  $f_r$ . These per-element diagrams are assumed known. They will typically have been derived from the precise on-ground characterization of the antenna array [22]. The power of the complex diagram is the antenna gain.

The azimuth variant propagation direction towards the target is defined in the so-called *element coordinate system*, which is related to the instrument coordinate system by a rotation  $\mathbf{R}_{I \rightarrow e}$ . The rotation accounts for, and is defined in terms of, the *antenna element mount angles*

$$\Delta \vec{\mathbf{A}}_e = (\Delta roll_e, \Delta pitch_e, \Delta yaw_e), \quad (7)$$

which represent the mispointing of each antenna element  $e$ . These angles are initially unknown and assumed zero.

The expected target backscatter amplitude  $R_{pq}^s(az, f_r)$  is accounted for in a similar fashion to the antenna pattern. The target amplitude varies as a function of the azimuth-variant propagation direction towards the sensor. It also depends on the polarization state of the transmit and receive antenna elements and varies as a function of the range frequency. It may also be complex valued if the reference target is known to be not an ideal point-like scatterer. The power of the modeled target backscatter is the radar cross section in  $\text{m}^2$ .

The backscatter model of each target is assumed known and may be directly measured, derived from electromagnetic simulations or analytically from geometric optics [23]. In addition to the backscatter model, the computation of  $R_{pq}^s(az, f_r)$  requires geometric transforms into a suitable reference target coordinate system. This coordinate system is the analog of the antenna element coordinate system introduced above. Details of the model used and the coordinate systems adopted are, however, beyond the scope of this article.

### 3.2. Response Analysis

To provide the inputs required for estimating calibration corrections, the measured target response is compared to the expected target response of (4), as illustrated in Figure 2. Any systematic discrepancy is potentially a sensor calibration issue that should be addressed by estimating corresponding calibration corrections. Such discrepancies will be termed residual errors in the following.

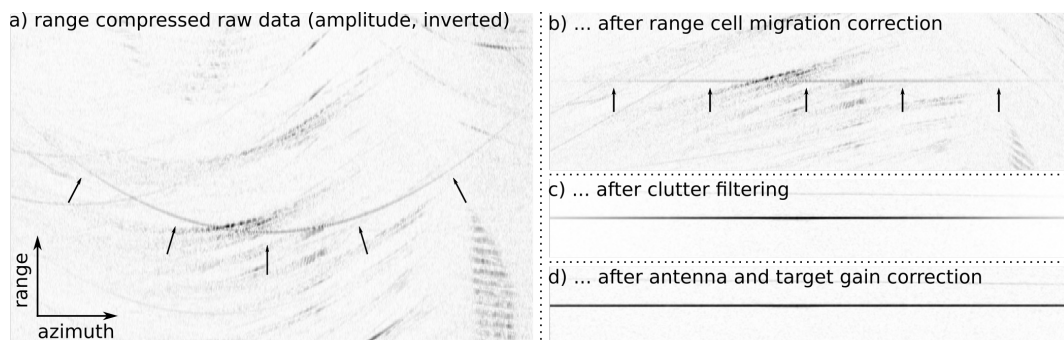


**Figure 2.** An illustration of the processing steps involved in the analysis of the response of a 1.5 m trihedral reflector in SAR data acquired at L-band in VV polarisation.

For a given data channel that uses antenna elements  $p$  and  $q$  to transmit and receive echos, respectively, the sensor acquires a 2D echo buffer  $D_{pq}(az, rg)$  defined over range and azimuth sample indices  $rg$  and  $az$ , respectively. The normalized response of a target  $s$  is closely related to residual errors in the response. It is given by

$$D_{pq}^s(az, rg) = \text{IFFT}_{f_r \rightarrow rg} \left[ \frac{\text{FFT}_{rg \rightarrow f_r} [D_{pq}(az, rg)]}{C_{pq}(az, f_r) M_{pq}^s(az, f_r)} \right], \quad (8)$$

where FFT and IFFT denote the forward and inverse discrete Fourier transform, respectively.  $M_{pq}^s(az, f_r)$  is the expected target response, defined in terms of the physical range frequency  $f_r$  in (4), while  $C_{pq}(az, f_r)$  is a correction derived from the composition of internal calibration measurements and external calibration corrections:

$$C_{pq}(az, f_r) = \text{FFT}_{rg \rightarrow f_r} [C_{pq}(az, rg)] \Delta C_{pq}(f_r). \quad (9)$$

In the above,  $C_{pq}(az, rg)$  is a 2D buffer of internal calibration pulses recorded alongside the data channel in question. In practice, the SAR sensor might not record an internal calibration signal for each and every pulse. The calibration buffer would then have to be interpolated in azimuth. Alternatively, internal calibration information may not be acquired during the actual data take at all. In this case, the calibration signal takes the form of a 1D chirp replica that is constant over azimuth.  $\Delta C_{pq}(f_r)$ , meanwhile, is a one dimensional, complex valued correction to the range frequency response. This correction is initially unknown and assumed equal to unity until estimates become available during the calibration process.

The application of Equation (8) simultaneously achieves all of the processing steps illustrated in Figure 2, apart from the clutter filtering. In view of implementation, it should be noted that the footprint of each individual target is typically relatively small. The calibration process can therefore be speeded up considerably by cropping the data analysed for each target. The azimuth extent of the response can, for example, be limited by thresholding  $\int |M_{pq}^s(az, f_r)|^2 df_r$ . Corresponding range limits are then given by the extrema of  $|\vec{r}_e^s(az)|$  within the valid azimuth extent.

To improve the signal to clutter ratio in the target response, analysis also includes an azimuth-adaptive clutter filter. This filter effectively singles out the directions of arrival corresponding to the reference target. The impact of this filtering step is illustrated in the example response of Figure 3. The approach is based on the observation that, since the target phase history is flattened in (8), the Doppler frequency of the response is expected to be constant and close to zero. Significant clutter reduction can therefore be accomplished by simply applying a Gaussian bandpass filter in the Doppler frequency domain:

$$F_{pq}^s(az, rg) = \text{IFFT}_{f_a \rightarrow az} \left[ K(f_a) \text{FFT}_{az \rightarrow f_a} [D_{pq}^s(az, rg)] \right] \quad \text{with} \quad K(f_a) = e^{-\frac{(f_a - \mu)^2}{2\sigma^2}}. \quad (10)$$

The filter mean  $\mu$  is set to coincide with the peak of the power spectrum of  $\sum_{rg} D_{pq}^s(az, rg)$ . The standard deviation  $\sigma$  is set to a value that preserves a certain angular resolution  $\delta\beta$  in the filtered response. The angular resolution may be defined relative to the overall angular response width in azimuth

$$\Delta\beta_{pq}^s = \frac{1}{2} \sum_{e \in \{p,q\}} \sum_{az} \arccos \left( 1 - \left| \vec{los}_e^s(az) \cdot \frac{\partial}{\partial az} \vec{los}_e^s(az) \right| \right) \quad (11)$$

such that

$$\sigma = \frac{\Delta\beta_{pq}^s}{\delta\beta}. \quad (12)$$

The results shown in this section and elsewhere in the paper are based on an angular resolution  $\delta\beta = 0.25^\circ$ .

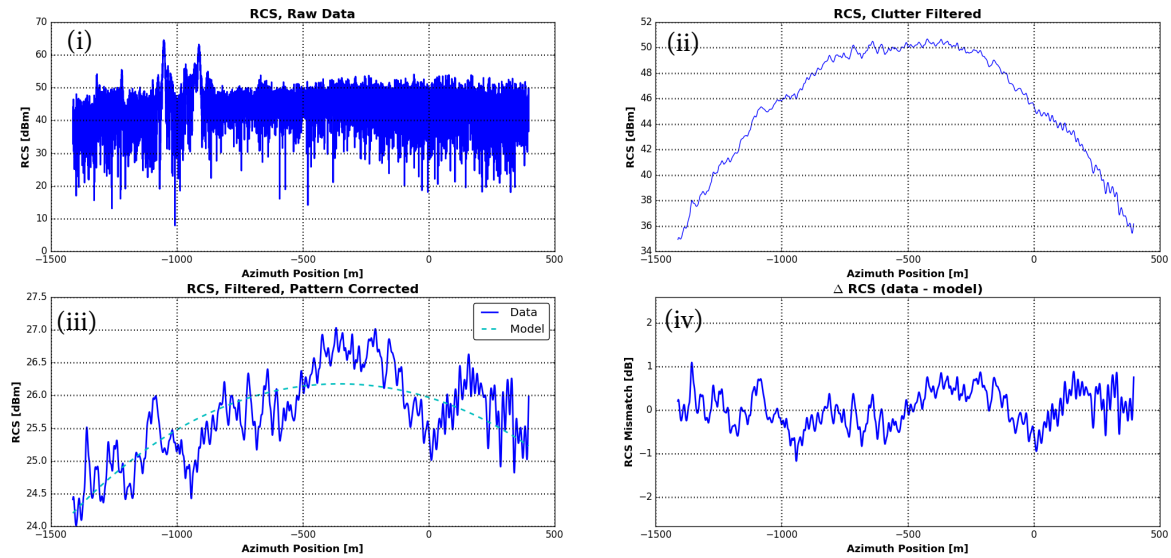


**Figure 3.** The impact on various analysis steps on the target Radar Cross Section (RCS) over azimuth, for the target of Figure 2. From top to bottom and left to right: (i) The backscatter intensity along the hyperbolic target range history in the original raw data. (ii) The target intensity after clutter filtering. (iii) The target intensity after the transmit and receive antenna patterns have been accounted for and, as a dotted line, the expected target RCS variation. (iv) The residual RCS offset between the expected and the measured target response.

Finally, accurate radiometric calibration requires an estimate of the clutter energy remaining in the reference target response after filtering. To this end, the average clutter energy per bin is robustly estimated in the azimuth frequency domain. It is defined as the median intensity between two and three kernel standard deviations offset from the peak response:

$$\text{Clutter}_{pq}^s = \left( \sum_{f_a} K(f_a)^2 \right) \text{median}_{2\sigma < |f_a - \mu| < 3\sigma} \left( \sum_{r_g} |D_{pq}^s(az, rg)|^2 \right) \quad (13)$$

### 3.3. Residual Errors

After the expected target response has been accounted for, the analysis result comprises residual errors, i.e., deviations from the expectation, for all combinations of reference target  $s$  and data channel  $pq$ : residual intensity variations  $\delta \text{RCS}_{pq}^s(az)$ , residual phase variations  $\delta \phi_{pq}^s(az)$  and residual range delays  $\delta \tau_{pq}^s(az)$ .

The residual  $\delta \text{RCS}_{pq}^s(az)$  measures the absolute, unit-less offset, in dB, between the expected and the measured RCS of the reference target. This offset is illustrated in the bottom right plot of Figure 3. Equation (8) has accounted for expected systematic intensity variations due to antenna element illumination patterns and the expected target RCS. In addition, the derivation of the absolute RCS offset from the filtered data  $F_{pq}^s(az, rg)$  of (10) must also consider the residual clutter intensity of Equation (13) as follows:

$$\delta \text{RCS}_{pq}^s(az) = 10 \log_{10} \left[ \left( \sum_{r_g} |F_{pq}^s(az, rg)|^2 \right) - \text{Clutter}_{pq}^s \right]. \quad (14)$$

The residual phase  $\delta \phi_{pq}^s(az)$ , meanwhile, measures phase errors in the target response that can be attributed to target range errors. The sensor position is affected by inaccuracies in the navigation

data and the antenna element phase center positions. Similarly, there is a residual uncertainty in the assumed reference target position on ground.

$$\delta\phi_{pq}^s(az) = \arg \left( \sum_{rg} F_{pq}^s(az, rg) \right) \quad (15)$$

In addition to the phase error above, the target range error can be measured directly. This residual delay is given by the offset of the target peak response away from the expected range. After the range cell migration correction of Equation (8), the expected peak is in the origin at  $rg = 0$ , such that the residual delay is estimated as

$$\delta\tau_{pq}^s(az) = \frac{1}{RSF} \arg \max_{rg} \left( \left| F_{pq}^s(az, rg) \right|^2 \right), \quad (16)$$

where  $RSF$  denotes the range sampling frequency of the raw data. The peak response is localized with sub-sample accuracy using the spectral diversity co-registration method described in [24] using a delta impulse  $\delta(rg)$  as a reference signal.

The residual phase of (15) and the residual delay of (16) measure essentially the same residual error and, in a certain sense, are complimentary: the phase measurement extremely sensitive but is relative in the sense that it is arbitrarily offset and wrapped in the interval  $[-\pi, \pi]$ . The residual delay, on the other hand, is less sensitive but does represent an absolute error. In an attempt to combine the advantages of both measures, the analysis derives the so-called absolute residual phase. It is defined as the offset, unwrapped residual phase:

$$\delta\chi_{pq}^s(az) = \chi_0 + \sum_{az} \arg \left( e^{j \frac{\partial}{\partial az} \delta\phi_{pq}^s(az)} \right) \quad (17)$$

The absolute phase offset  $\chi_0$  is set to ensure consistency with the residual delay by enforcing the equality

$$\text{median}_{az} \left( \delta\chi_{pq}^s(az) + 2\pi f_0 \delta\tau_{pq}^s(az) \right) = 0, \quad (18)$$

where  $f_0$  denotes the radar center frequency. Figure 4 illustrates the information content of the residual phase, the residual delay and the absolute residual phase.

Finally, the calibration approach also uses the so-called target coherence. It quantifies the reliability of the response characterization over azimuth. The coherence is close to one for clean portions of the target response and decreases towards zero where the response is perturbed by residual clutter, system noise or Radio Frequency Interference (RFI). It is denoted  $w_{pq}^s(az)$ , as it is principally used as a weight when deriving calibration corrections, and is defined as

$$w_{pq}^s(az) = \left| e^{j \delta\phi_{pq}^s(az)} \otimes S(az) \right| \quad (19)$$

where  $\otimes$  denotes convolution and  $S(az)$  is a low-pass filter that is narrow enough to provide an unbiased coherence estimate. The convolution may, for example, correspond to a moving average window with a size on the order of  $\sim 100$  samples.



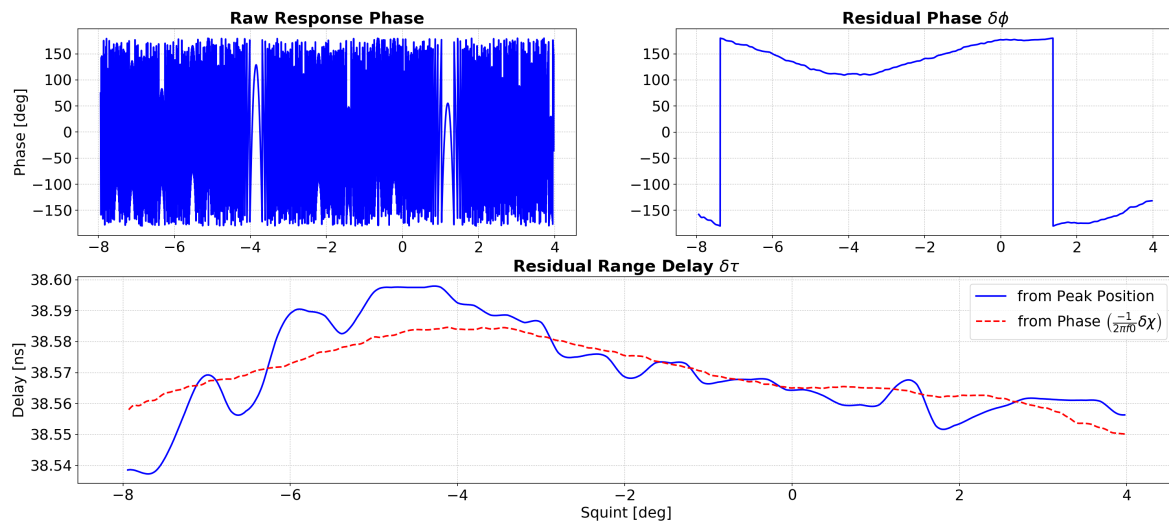


**Figure 4.** The results of phase and delay analysis for the target shown in Figure 2, imaged at X-band with a bandwidth of 384 MHz. The two plots in the top row show the original phase in the raw data (left) and the wrapped residual phase  $\delta\phi_{pq}^s(az)$ , obtained after the expected target phase has been removed from the raw response (right). The plot in the bottom row illustrates the consistency of the residual delay  $\delta\tau_{pq}^s(az)$  and the absolute residual phase  $\delta\chi_{pq}^s(az)$ .

#### 4. Model-Based Calibration

Calibration proceeds on the basis of residual errors identified in the reference target responses. It entails introducing corrections to sensor parameters that aim to minimize these errors. External calibration thus becomes a rigorous optimization process: explicit models link sensor properties to the expected target response. Appropriate sensor parameter corrections are then the result of error minimization by model inversion.

To make this inversion robust to outliers caused by RFI, system noise and other transient effects, model inversion uses L1-norm error minimization [25] in favor of least-squares approaches throughout. Given an error functional  $E_{pq}^s(az)$  that measures some model mismatch over azimuth, L1-norm optimization yields a set of model parameters  $\mathcal{O} = \{o_1, o_2, \dots\}$  that are the solution to

$$\arg \min_{\mathcal{O}} \left( \sum_{az, pq, s} |E_{pq}^s(az)| \right), \quad (20)$$

where errors are summed over all target responses in all data channels of all acquisitions.

To ensure that the optimization problem is convex, the following sections uses a closely related objective function

$$\arg \min_{\mathcal{O}} \left( \sum_{az, pq, s} \Psi(E_{pq}^s(az)^2) \right) \text{ with } \Psi(e) = \sqrt{e + \epsilon}, \quad (21)$$

where  $\epsilon$  is introduced only to ensure numerical stability and is set to  $1 \times 10^{-8}$ . The convexity of this function guarantees convergence to a global minimum. The minimisation of (21) is achieved by setting the derivative of the total error with respect to each model parameter  $o_i \in \mathcal{O}$  to zero, such that

$$\forall o_i \in \mathcal{O} : 0 = \sum_{az, pq, s} \frac{\partial \Psi(E_{pq}^s(az)^2)}{\partial o_i} = \sum_{az, pq, s} \dot{\Psi} E_{pq}^s(az) \frac{\partial E_{pq}^s(az)}{\partial o_i}, \quad (22)$$

where  $\dot{\Psi} = (E_{pq}^s(az)^2 + \epsilon)^{-\frac{1}{2}}$ .

While this system of equations is clearly non-linear, it can be solved using a fixed point iteration. In each iteration,  $\hat{\Psi}$  is pre-computed on the basis of the currently available parameter estimates  $\hat{\mathcal{O}}$ .  $\hat{\Psi}$  is then treated as a constant in the solution of (22) and new, refined model parameter estimates are obtained. This process is repeated for a fixed number of iterations (e.g., 10) or until the model parameters have converged.

#### 4.1. Range Impulse Response

The aim of the residual range impulse response calibration is to measure systematic, amplitude and non-linear phase variations as illustrated in Figure 5. Such variations occur within the pulse bandwidth when internal calibration measurements fail to faithfully reproduce the transfer function of the radar instrument.

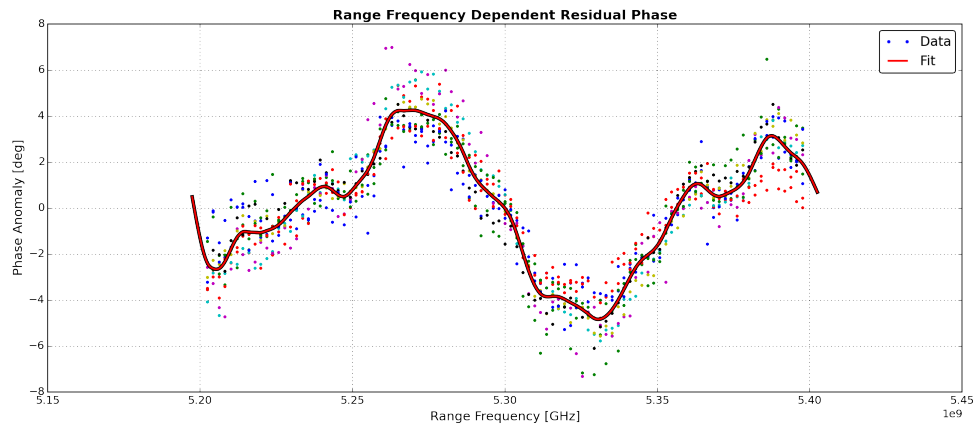


**Figure 5.** The phase of the C-band VV-pol range IRF estimated from a data comprising the range histories of reference targets in multiple calibration acquisitions. The solid line indicates the estimated correction. It is used to compensate for the systematic variations observed as a function of radar frequency. A similar analysis is carried out for the IRF amplitude.

Estimation begins with pre-processing the filtered raw data to remove constant offsets in gain and residual delay as follows:

$$H_{pq}^s(az, f_r) = \text{FFT}_{rg \rightarrow f_r} \left[ \frac{F_{pq}^s(az, rg)}{\sqrt{\sum_{rg} |F_{pq}^s(az, rg)|^2}} \right] \exp \left( \frac{-j f_r}{f_0} \delta \chi_{pq}^s(az) \right). \quad (23)$$

The gain and phase of transfer function corrections are estimated independently. Each combination of antenna elements  $pq$  is thereby associated with corrections  $\Delta C_{pq}^{gain}(f_r)$  and  $\Delta C_{pq}^{phase}(f_r)$  that constitute the parameter set  $\mathcal{O}$  in the corresponding optimization problem (21). The error measures used are

$$E_{pq}^{s,gain}(az, f_r) = w_{pq}^s(az) \left( 20 \log_{10} \left( |H_{pq}^s(az, f_r)| \right) - \Delta C_{pq}^{gain}(f_r) \right) \quad (24)$$

and

$$E_{pq}^{s,phase}(az, f_r) = w_{pq}^s(az) \left( \arg \left( \frac{H_{pq}^s(az, f_r)}{\sum_{f_r} H_{pq}^s(az, f_r)} \right) - \Delta C_{pq}^{phase}(f_r) \right), \quad (25)$$

where the coherence  $w_{pq}^s(az)$  of Equation (19) is used to emphasize the influence of reliable measurements in the estimated corrections.

The iterative solution of (22) achieves a robust fit over all pulses in each target response and involves two equations for each discrete range frequency  $f_r$ , one related to  $\Delta C_{pq}^{gain}(f_r)$  and one related

to  $\Delta C_{pq}^{phase}(f_r)$ . Upon convergence, the complex valued impulse response correction for the antenna element combination  $pq$  is given by

$$\Delta C_{pq}(f_r) = 10^{\frac{\Delta C_{pq}^{gain}(f_r)}{20}} e^{j\Delta C_{pq}^{phase}(f_r)}. \quad (26)$$

After residual range frequency response corrections have been obtained, reference target analysis is repeated, as shown in Figure 1, where these corrections are taken into account in Equation (9).

#### 4.2. Antenna Mispointing

The aim of the element mispointing estimation is to derive optimal values for the roll/pitch/yaw corrections introduced in Equation (7). These are the Euler angles underlying the rotation matrix  $\mathbf{R}_{I \rightarrow e}$  that transforms instrument to antenna element coordinates in the antenna model of Equation (6).

The proposed pointing calibration yields attitude angle corrections that minimize variations in the RCS errors  $\delta \text{RCS}_{pq}^s(az)$  of Equation (14). The underlying model aims to explain the residual RCS mismatch as a mispointing of individual antenna elements plus a constant gain offset. The corresponding error function takes the form

$$E_{pq}^{s,\Delta A}(az) = w_{pq}^s(az) \left( \delta \text{RCS}_{pq}^s(az) - \Delta \text{RCS}_{pq} - \sum_{e \in \{p,q\}} \Delta \text{Gain}_e^s(az) \right) \quad (27)$$

where  $\Delta \text{RCS}_{pq}$  is an unknown constant gain offset characteristic of the channel  $pq$ , and  $\Delta \text{Gain}_e^s(az)$  denotes the overall, azimuth variant change in the antenna gain, in dB, due to the pointing correction  $\Delta \vec{A}_e$ . The gain change is derived from the two-way complex antenna gain  $A_{pq}^s(az, f_r)$  of Equation (6) as follows:

$$\Delta \text{Gain}_e^s(az) = 10 \log_{10} \left( \frac{\sum_{f_r} |A_{pq}^s(az, f_r)|^2}{\sum_{f_r} |A_{pq}^s(az, f_r | \Delta \vec{A}_e = \vec{0})|^2} \right), \quad (28)$$

where the summations over  $f_r$  are over the radar signal bandwidth and  $A_{pq}^s(az, f_r | \Delta \vec{A}_e = \vec{0})$  denotes the nominal complex antenna gain obtained when all pointing correction angles are left at zero.

The minimization of errors of the form (27) is complicated by the non-linearity of Equation (28) with respect to the unknown attitude corrections  $\Delta \vec{A}_e$ . The non-linearity is circumvented by linearizing the error function (27) to obtain

$$\hat{E}_{pq}^{s,\Delta A}(az) = w_{pq}^s(az) \left( \delta \text{RCS}_{pq}^s(az) - \Delta \text{RCS}_{pq} - \sum_{e \in \{p,q\}} \Delta \text{Gain}_e^s(az) + \vec{\mathcal{G}}_e^s(az) \cdot \vec{\delta}_e^{r,p,y} \right), \quad (29)$$

in which  $\vec{\delta}_e^{r,p,y} = (\delta_e^{roll}, \delta_e^{pitch}, \delta_e^{yaw})$  denote unknown incremental refinements to the current mispointing estimate  $\Delta \vec{A}_e$ , and  $\vec{\mathcal{G}}_e^s(az)$  contains the corresponding, azimuth variant derivatives of  $\Delta \text{Gain}_e^s(az)$  with respect to the three angular axes. These derivatives are obtained numerically from the change in  $\Delta \text{Gain}_e^s(az)$  when the current estimate  $\vec{\mathcal{G}}_e^s(az)$  is perturbed in each dimension.

The system of Equation (22) used for minimization comprises three equations for each antenna element  $e$ , with one equation for each angular axis. In addition, it includes one equation corresponding to the constant unknown gain offset in each channel  $pq$ . After each step of the fixed point iteration, the corrections  $\vec{\delta}_e^{r,p,y}$  are applied additively to the current  $\Delta \vec{A}_e$  estimate and the values of  $\Delta \text{Gain}_e^s(az)$  and the numerical gradients  $\vec{\mathcal{G}}_e^s(az)$  are updated accordingly. As indicated in Figure 1, target analysis is repeated to take into account the estimated pointing corrections in (6). Figure 6 illustrates this optimization process. It shows how a pointing estimate minimizes the mismatch between the expected and the measured reference target RCS.

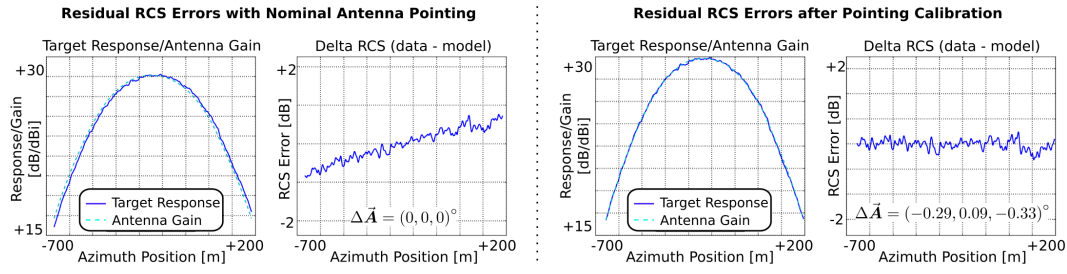


**Figure 6.** The impact of antenna pointing calibration on the residual RCS errors along azimuth, illustrated by the response of a single 1.5 m trihedral reflector imaged at C-band in VV polarization. The sub-plots show a superposition of the target backscatter intensity without antenna pattern correction and the antenna gain (left) and the residual RCS error  $\delta\text{RCS}_{pq}^s(\text{az})$ .

#### 4.3. Phase Center Positions and Troposphere

Phase center calibration aims to improve the accuracy of the assumed absolute antenna element phase center positions, as parameterized by the vector  $\vec{L}_e$  introduced in the context of (2). In addition, this calibration step provides an estimate for the residual tropospheric propagation delay  $\Delta c$  introduced in Equation (5). The latter allows corrections to phase center geometry to be clearly separated from other effects. In practice, it may be used to discover any systematic error in the assumed value of  $c$  or, when estimated corrections are unreasonably large or highly variable, instabilities in the assumed radar center frequency. It should be noted that, while this approach is sufficient in airborne SAR applications, it would have to be extended to consider ionospheric effects in low frequency/large wavelength space borne scenarios [26].

The underlying model relates phase center corrections  $\Delta\vec{L}_e$  and the tropospheric propagation correction  $\Delta c$  to the observed absolute residual phase of Equation (17). The corresponding error function to be minimized is given by

$$E_{pq}^{s,\Delta L}(\text{az}) = \frac{(1 + \Delta c) \lambda}{2\pi} \delta\chi_{pq}^s(\text{az}) - \Delta c \sum_{e \in \{p,q\}} |\vec{r}_e^s(\text{az})| + \Delta\text{los}_{pq}^s(\text{az}) - \Delta r_{pq}, \quad (30)$$

where  $\lambda = \frac{c}{f_0}$ ,  $\Delta r_{pq}$  is a constant range offset that is related to residual propagation delays within the sensor, and

$$\Delta\text{los}_{pq}^s(\text{az}) = \sum_{e \in \{p,q\}} \vec{\text{los}}_e^s(\text{az}) \cdot \Delta\vec{L}_e \quad (31)$$

is the range offset corresponding to position corrections  $\Delta\vec{L}_e$  projected onto the line of sight vectors  $\vec{\text{los}}_e^s(\text{az})$  defined in (3).

While the error measure (30) aims to introduce corrections that minimize the absolute phase mismatch, it fails to capture an important property of multi-channel SAR: after calibration, any residual errors must be identical in all of the data channels comprising a single acquisition. All channels are equally affected by inaccuracies in the assumed sensor or target positions. To capture this prior knowledge, phase center calibration introduces a second, additional error measure

$$E_{pq,uv}^{s,\Delta L}(\text{az}) = E_{pq}^{s,\Delta L}(\text{az}) - E_{uv}^{s,\Delta L}\left(t_{uv}^{-1}(t_{pq}(\text{az}))\right) \quad (32)$$

that penalizes any difference in the residual mismatch between two simultaneously acquired channels  $pq$  and  $uv$ . The composed mapping  $t_{uv}^{-1}(t_{pq}(\text{az}))$  serves to co-register the channels  $uv$  and  $pq$  using the relation between azimuth index and continuous time introduced in the context of (2).

To accommodate the additional differential error (32) as well as the coherence weight  $w_{pq}^s(az)$  of (19), the fixed point iteration of (22) is modified to include a second summation over simultaneously acquired pairs of channels  $(pq, uv)$ :

$$\forall o_i \in \mathcal{O} : 0 = \sum_{az, pq, s} w_{pq}^s(az) \frac{\partial \Psi(E_{pq}^{s, \Delta L}(az)^2)}{\partial o_i} + \sum_{az, (pq, uv), s} w_{pq, uv}^s(az) \frac{\partial \Psi(E_{pq, uv}^{s, \Delta L}(az)^2)}{\partial o_i}, \quad (33)$$

where

$$w_{pq, uv}^s(az) = w_{pq}^s(az) w_{uv}^s(t_{uv}^{-1}(t_{pq}(az))). \quad (34)$$

Generalizing the pattern of (22), each iteration involves pre-computing two  $\Psi$  terms, one for each error measure. The parameter set  $\mathcal{O}$  comprises the tropospheric propagation correction  $\Delta c$ , the corrections  $\Delta \vec{L}_e$  for all antenna elements  $e$  as well as channel dependent, constant range offsets  $\Delta r_{pq}$ .

#### 4.4. Interferometric Baselines

The calibration procedure described in the preceding section yields refined estimates of the absolute antenna element phase centers. These estimates are sufficient to provide consistently high geometric accuracy in the focused SAR imagery. They are still less accurate, however, than the limit set by residual errors in the assumed sensor and reference target positions. This residual inaccuracy is on the order of a few centimetres for position information derived from differential Global Positioning System (GPS) measurements. As such, it is still far too large for interferometric applications. In interferometry, phase differences, rather than absolute positions, are of central importance.

This section introduces a calibration procedure that precisely determines interferometric baselines, i.e., the spatial separation of antenna element phase centers, to ensure phase consistency among all the channels of a multi-channel SAR sensor. Baseline calibration, as illustrated in Figure 7, is based on the residual interferometric phase between two simultaneously acquired data channels  $pq$  and  $uv$ . It is obtained as

$$\delta \phi_{pq, uv}^s(az) = \arg \left( e^{j \delta \phi_{pq}^s(az)} e^{j \delta \phi_{uv}^s(t_{uv}^{-1}(t_{pq}(az)))} \right), \quad (35)$$

where  $\delta \phi_{pq}^s(az)$  denotes the residual phase of (15) and  $t_{uv}^{-1}(t_{pq}(az))$  is used to achieve the co-registration of the channels  $pq$  and  $uv$  in time, as in (32). For a given channel combination  $(pq, uv)$ , this results in a set of phase vectors

$$\left\{ \delta \phi_{pq, uv}^1(az), \delta \phi_{pq, uv}^2(az), \dots \right\} \quad (36)$$

corresponding to all available reference targets  $s = 1, 2, \dots$ . To be of use in 3D baseline refinement, these phase differences must be made consistent by unwrapping them. To this end, each phase measurement  $\delta \phi_{pq, uv}^s(az)$  is associated with a 2D coordinate

$$\left( \alpha_p^s(az, \Delta \vec{A}_p), \beta_p^s(az, \Delta \vec{A}_p) \right) \mapsto \delta \phi_{pq, uv}^s(az) \quad (37)$$

that parameterizes the azimuth variant angular propagation direction towards the target as in Equation (6). Once the interferometric phase measurements comprising a set such as that of (36) have been thus embedded in the 2D angular domain, a phase unwrapping algorithm for sparse grids (In view of phase offset calibration, described in Section 4.5, the unwrapping process should only add or subtract multiples of  $2\pi$  and not introduce arbitrary phase offsets.), for example [27] or [28], is applied to obtain unwrapped phase vectors

$$\left\{ \delta \phi_{pq, uv}^{1, UW}(az), \delta \phi_{pq, uv}^{2, UW}(az), \dots \right\}. \quad (38)$$



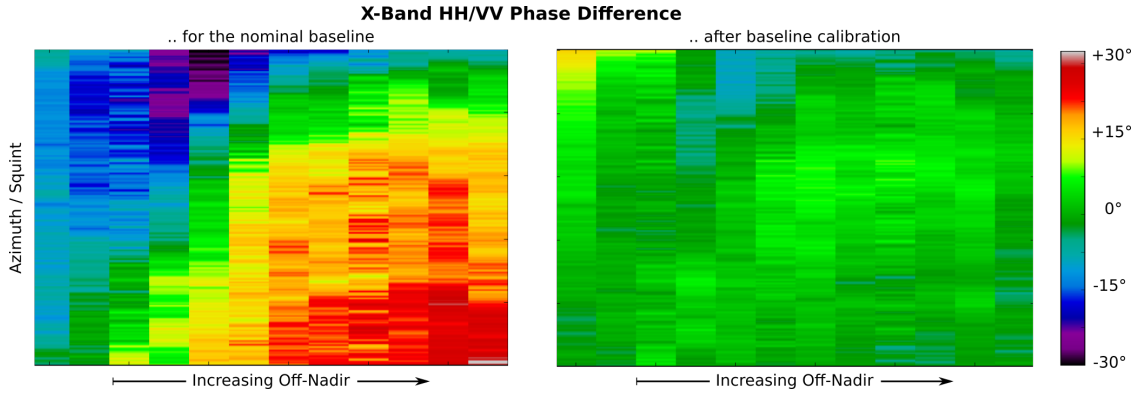


**Figure 7.** An illustration of how baseline calibration addresses systematic errors in the polarimetric phase. The plots show the impact of adjusting the spatial separation of the H and V phase centers of the primary F-SAR X-band antenna. Each image shows the HH/VV phase difference measured, in a single acquisition, over 12 trihedral reflectors. Each column shows the phase difference within the range history of a single reflector. Reflectors (columns) are arranged in order of increasing off-nadir angle. The difference between the left and right plots corresponds to a baseline refinement of only (3.4, 0.8, 0.1) mm in the instrument coordinate system.

The error model functional  $E_{pq,uv}^{s,BL}(az)$  used for baseline refinement aims to minimize residual interferometric phase errors  $\delta\phi_{pq,uv}^{s,UW}(az)$  by introducing antenna element phase center position adjustments  $\Delta\vec{L}_e^{BL}$ , which are incremental refinements of the corrections  $\Delta\vec{L}_e$  introduced in the previous section.

$$E_{pq,uv}^{s,BL}(az) = w_{pq,uv}^s(az) \left( \delta\phi_{pq,uv}^{s,UW}(az) + \frac{2\pi f_0}{(1 + \Delta c)c} \Delta los_{pq,uv}^s(az) - \Delta\phi_{pq,uv} \right), \quad (39)$$

where

$$\Delta los_{pq,uv}^s(az) = \sum_{e \in \{p,q\}} \vec{los}_e^s(az) \cdot \Delta\vec{L}_e^{BL} - \sum_{e \in \{u,v\}} \vec{los}_e^s(t_{uv}^{-1}(t_{pq}(az))) \cdot \Delta\vec{L}_e^{BL} \quad (40)$$

denotes the azimuth variant, cumulative change in line of sight distance to the reference target  $s$  due to lever arm corrections  $\Delta\vec{L}_e^{BL}$  with  $e \in \{p, q, u, v\}$ . The variable  $\Delta\phi_{pq,uv}$  absorbs arbitrary constant phase offsets specific to the channel combination under consideration, while the differential coherence weight  $w_{pq,uv}^s(az)$  is defined in (34).

As in the case of (33), the fixed point iteration of (22) must be modified to accommodate the summation over pairs of channels  $(pq, uv)$ . In addition, interferometric baseline calibration deals only in channel differences and is ill-posed unless the optimization is further constrained. To this end, the optimization includes an additional penalty for displacements of the geometric centre of the antenna array:

$$\langle L_e^{BL} \rangle^2 = 0 \quad \text{where} \quad \langle L_e^{BL} \rangle = \sum_e \Delta\vec{L}_e^{BL}. \quad (41)$$

The fixed point iteration for baseline calibration, including the constraint above, therefore uses a system of equations

$$\forall o_i \in \mathcal{O} : 0 = 2 \langle L_e^{BL} \rangle \frac{\partial \langle L_e^{BL} \rangle}{\partial o_i} + \sum_{az, (pq, uv), s} \frac{\partial \Psi(E_{pq,uv}^{s, \Delta L}(az)^2)}{\partial o_i}, \quad (42)$$

where the set of model parameters  $\mathcal{O}$  comprises phase center position refinements  $\Delta\vec{L}_e^{BL}$  and constant phase offsets  $\Delta\phi_{pq,uv}$ . Note that the tropospheric propagation correction  $\Delta c$  retains the value estimated previously and is treated as a known constant during baseline calibration. After the fixed point

iteration has converged, the refinements  $\Delta \vec{L}_e^{BL}$  are added to the previously obtained phase center position corrections  $\Delta \vec{L}_e$ .

#### 4.5. Calibration Constants

The procedures described in the preceding sections have provided range frequency and propagation direction dependent corrections. The last step in the external calibration is then to introduce calibration constants. These account for systematic offsets in gain, delay and phase that are inherent to the sensor and are not related to the physical characteristics of the imaged scene.

Indeed, such constants have already been estimated: gain offsets  $\Delta \text{RCS}_{pq}$ , range offsets  $\Delta r_{pq}$  and phase offsets  $\Delta \phi_{pq,uv}$  are byproducts of the minimization of error measures (29), (30) and (39), respectively. As corrections are introduced sequentially, however, gain and delay offsets need to be re-estimated to ensure consistency. Robust re-estimation is accomplished by solving minimization problems of the form (21) for simplified versions of the error measures (29) and (30). Simplification entails symbolically substituting  $\vec{\delta}_e^{r,p,y} = 0$  and  $\Delta \vec{L}_e = 0$ , such that the model parameter sets  $\mathcal{O}$  are reduced to the calibration constants of interest.

While the calibration constants  $\Delta \text{RCS}_{pq}$  and  $\Delta r_{pq}$  can be easily and conveniently applied to the raw data of each channel  $pq$  before SAR focusing, the phase calibration constants  $\Delta \phi_{pq,uv}$  would have to be applied each time an interferogram is formed. In practice, it is therefore desirable to derive phase calibration information for individual channels, such that

$$\Delta \phi_{pq} + \Delta \phi_{uv} = \Delta \phi_{pq,uv}. \quad (43)$$

Solving this system of equations is not straight-forward due the fact that the interferometric phase is wrapped. Constants for individual channels can, however, be obtained by constructing a graph with nodes  $\Delta \phi_{pq}, \Delta \phi_{uv}, \dots$  connected by directed edges associated with phase differences  $\Delta \phi_{pq,uv}$ . A phase unwrapping algorithm for arbitrary grids, such as [27,28], can then be used to obtain the desired individual channel calibration constants.

## 5. Results and Discussion

The calibration approach described in previous sections is part of the operational processing environment for DLR's multi-channel, airborne F-SAR [8] and DBFSAR [29] instruments. The external calibration of these sensors is an ongoing activity that is carried out several times each year to account for upgrades to the sensor hardware, the fact that the radar hardware as well as the antenna mounts need to be re-installed after the research aircraft has been engaged in other scientific activities and, last but not least, to regularly monitor the system stability throughout periods of scientific SAR data acquisition campaigns.

The external calibration of these sensors involves dedicated calibration data acquisitions over a calibration field that is permanently installed at the Kaufbeuren airfield in southern Germany. This installation comprises 9 trihedral radar reflectors ranging in leg-length from 0.9 m to 1.5 m, as well as a single dihedral reflector rotated by  $22.5^\circ$  in the line of sight to produce equally strong returns in the co- and cross-polarizations. The trihedral reflectors are deployed across the sensor swath at roughly equal intervals corresponding to off-nadir angles in the range  $32^\circ$  to  $55^\circ$ .

The results presented in the following sub-sections are, unless otherwise noted, based on SAR data acquired as part of the 2019 F-SAR calibration campaign *OP19AF* with 10 independent flights from February to June. Each flight comprises roughly 15 SAR acquisitions, in each of which several of the frequency bands X, C, S and L are acquired simultaneously. Almost all of the data acquired are fully polarimetric and some feature polarimetric single-pass interferometry at X- or S-band. The illustrations in Sections 3.2 and 4 are also derived from the raw data collected in this calibration campaign.

Each of the following four sub-sections highlights a particular type of calibration correction. The results presented aim to show how each correction improves the fidelity of SAR measurements.

In addition, the results illustrate the types of errors that can be corrected using the approaches developed. Furthermore, the experimental results show that the analyses carried out on range compressed raw data transfer to the focused SAR imagery. They also aim to show that such improvements represent external calibration. The corrections are seen to address systematic errors, rather than merely correcting for transient effects. This is accomplished by showing that results are consistent over multiple independent calibration data acquisitions. In other experiments, calibration corrections are seen to improve the quality of information derived from raw data acquired in the course of scientific measurement campaigns.

### 5.1. Radiometry

Other than the comparatively trivial constant gain offset of Section 4.5, the calibration process affects the radiometric accuracy of the processed SAR data through the pointing estimate  $\Delta\bar{A}_e$ . The impact of the antenna pointing correction is illustrated by the C-band examples of Figure 8 (One of the many responses shown in this Figure was also used as a basis for Figure 6 above.) In the polar plots of the first two rows, each reflector response is represented as a line in a coordinate system similar to (37): azimuth indices are mapped to a propagation direction. This direction is parameterized by squint and off-nadir angles in the antenna reference frame. The trajectories are non-linear and differ from acquisition to acquisition due to variations in the platform attitude angles. The plots in the third row, meanwhile, are based on the analysis of reference targets in focused SAR imagery. In these plots, each reference target is represented by a single data point. Lines connect all targets imaged within a single channel.

The polar plots in the left column clearly show a systematic RCS variation of  $\pm 1.5$  dB along azimuth, which is largely compensated for by the pointing correction introduced. By contrast, the evaluation in the third row is based on focused SAR data after azimuth compression. As such, it is therefore insensitive to large, systematic variations along the range history of targets. In this light, the estimated standard deviation of 0.3 dB in the bottom left plot is seen to be a gross misrepresentation. Instead, errors on the order of 1 dB are to be expected as the squint angle varies. Such variation is to be expected when data are acquired under different conditions in the field.

The plots in the right column show that the pointing estimate effectively reduces the systematic errors along azimuth. Indeed, it even reduces the RCS mismatch measured in the focused SAR data, as shown in the last row. The polar plots also show, however, that residual RCS errors, which cannot be attributed to antenna pointing, remain. The residual errors and their visualization are helpful in characterizing these types of errors and identifying potential causes. In this case, residual errors are possibly linked to an issue with the antenna pattern measurement.

Figure 9 illustrates the impact on antenna pointing calibration for data acquired by the DBFSAR sensor. The acquisitions were carried out over the Kaufbeuren calibration site during the *DATLAS* test flights of 2018. The results pertain to one of the channels of the six-phase center ATI/GMTI configuration of DBFSAR. They were acquired at X-band in VV polarization and with a bandwidth of 800 MHz. The sensor, in this particular configuration, uses a single transmit antenna with a narrow beam of  $2^\circ$  and six separate, wider receive antennas. The pointing calibration yields separate corrections for the transmit and receive antennas. As the Figure caption indicates, the transmit pointing correction is significant: it is comparable to the antenna beam width. The large correction is consistent with the large initial RCS mismatch observed. It is most likely due to a misalignment of the antenna during the on-ground measurement of the antenna pattern.

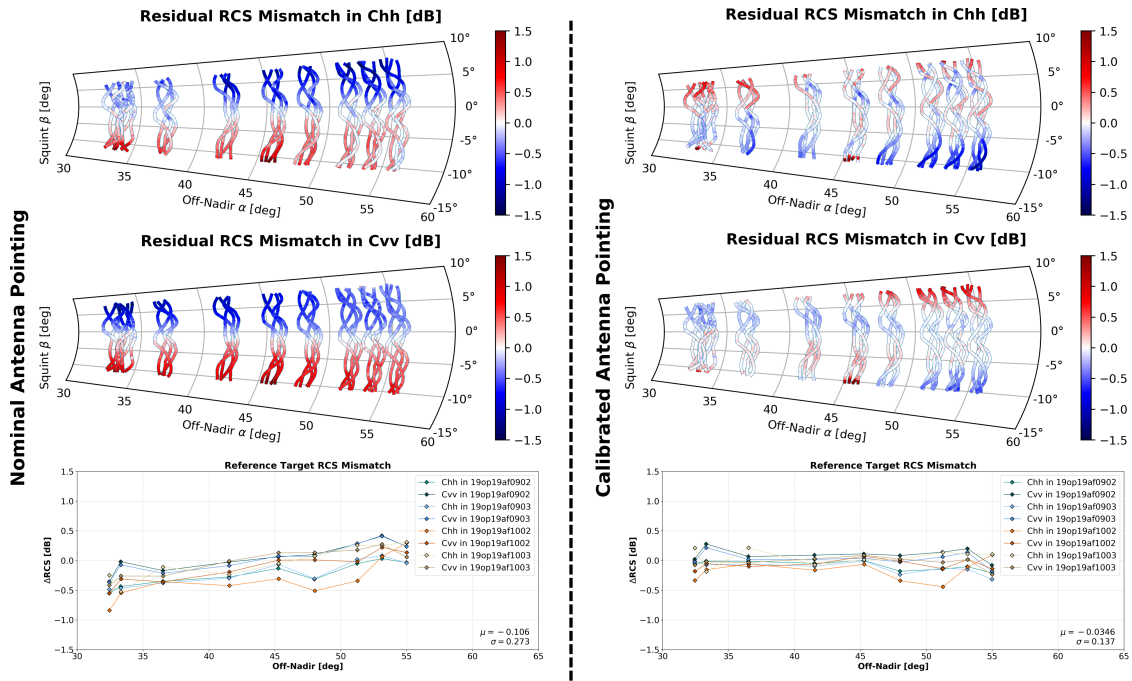


**Figure 8.** A comparison of RCS analysis results before and after C-band antenna pointing calibration. The first two rows visualize the residual RCS errors  $\delta RCS_{pq}^s(az)$  within the range history of reference targets in the co-polar channels of four independent calibration data acquisitions. The plots in the bottom row illustrate the corresponding RCS mismatch derived from the analysis of focused SAR imagery. The estimated, optimal pointing correction, which was constrained to be identical in  $H$  and  $V$ , amounted to  $(\Delta roll_e, \Delta pitch_e, \Delta yaw_e) = (-0.288^\circ, 0.00^\circ, -0.44^\circ)$ .

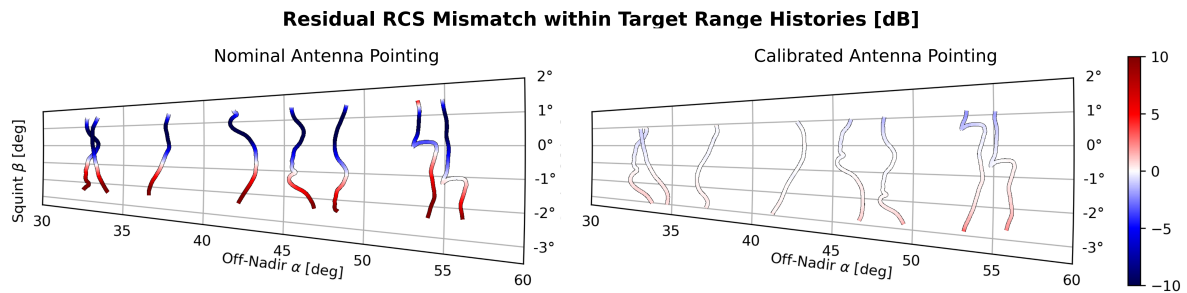


**Figure 9.** The impact of antenna pointing estimation and correction on the residual RCS mismatch. The plots illustrate variations observed within the range histories of trihedral reflectors imaged by DBFSAR at X-band. Large RCS errors (left) are much reduced when target analysis takes into account the estimated antenna pointing correction (right). Calibration yields independent pointing corrections for the transmit and receive antennas of  $\Delta A_T = (1.70^\circ, -1.58^\circ, 0.03^\circ)$  and  $\Delta A_R = (-0.03^\circ, -0.84^\circ, -0.09^\circ)$ , respectively.

Figure 10 shows the impact of this pointing estimate on focused imagery. These acquisitions took place over the city of Landsberg am Lech, Germany. Although there are no reference targets available for this site, the calibration quality is clearly improved when the estimated pointing correction is taken into account during the antenna pattern correction in SAR processing.



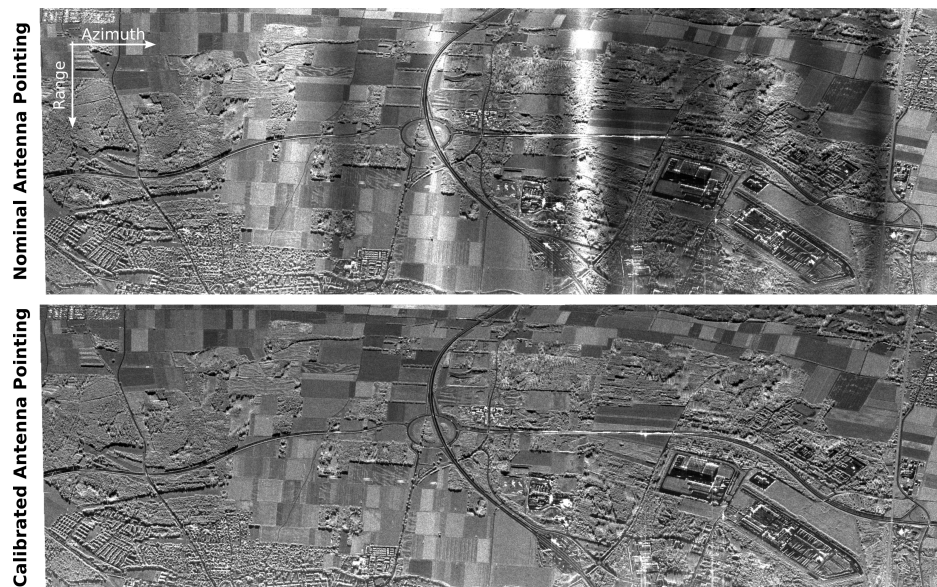


**Figure 10.** The impact of the pointing estimate of Figure 9 on the backscatter amplitude in an independent SAR acquisition over the city of Landsberg am Lech.

## 5.2. SAR Impulse Response Function

The proposed calibration approach also has an impact on the impulse response function achieved during SAR processing. Figure 11 illustrates the improvement achieved for a reference target imaged at C-band: the principal improvement lies in the flattening of the range spectral profile, shown in the middle column, which is due to the response correction introduced in Section 4.1. A further, but less significant improvement is due to the flattening of the azimuth spectral profile, shown on the right, which is due to the C-band antenna pointing correction that is illustrated in more detail in Figures 6 and 9.

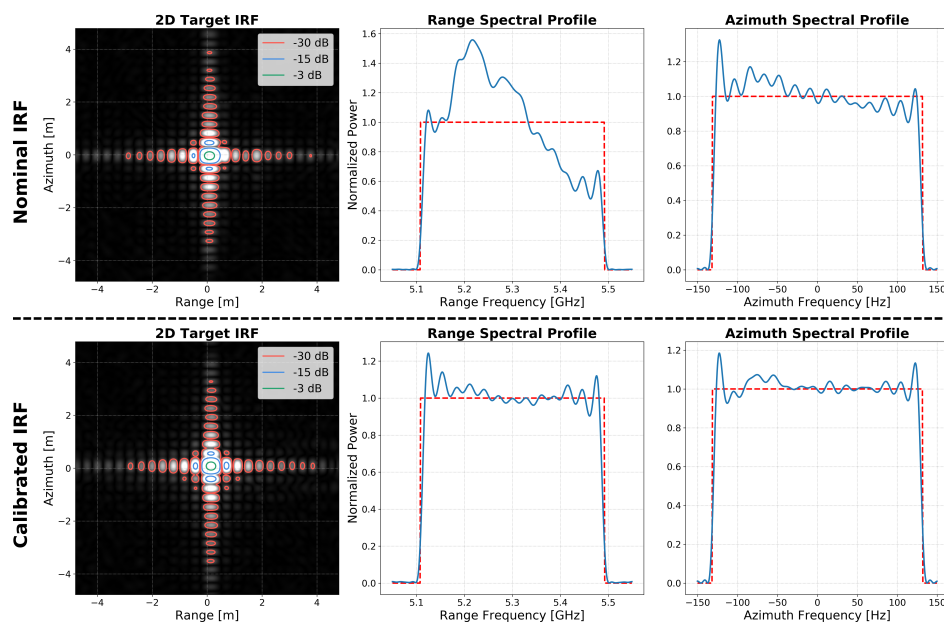


**Figure 11.** A comparison of the 2D SAR impulse response function of a reference target imaged in VV polarisation at C-band. The top row represents the nominal performance. The IRF in the bottom row, meanwhile, is the one obtained when the estimated calibration corrections are taken into account. The plots in the second and third columns show the normalized power spectrum in range and in azimuth. The red dashed lines indicate the signal bandwidth.



### 5.3. Geometric Accuracy

Sections 4.3 and 4.4 introduce corrections to the assumed multi-aperture antenna array geometry. While the baseline corrections of Section 4.4 establish inter-channel phase consistency and are generally small, the phase center positions refinements  $\Delta\vec{L}_e$  and tropospheric propagation correction  $\Delta c$  of Section 4.3 are potentially large and can have a measurable impact on the geometric accuracy of the focused SAR imagery.

Figure 12 illustrates the impact of antenna phase center calibration on a set of five independent polarimetric L-band acquisitions. The polar plots in the first two rows visualize absolute residual phase errors  $\delta\chi_{pq}^s(az)$  within the range histories of trihedral reflectors in the two co-polar channels. As implied by (18) and illustrated in Figure 4, these phase errors are directly related to residual range delay or, equivalently, range position mismatch.

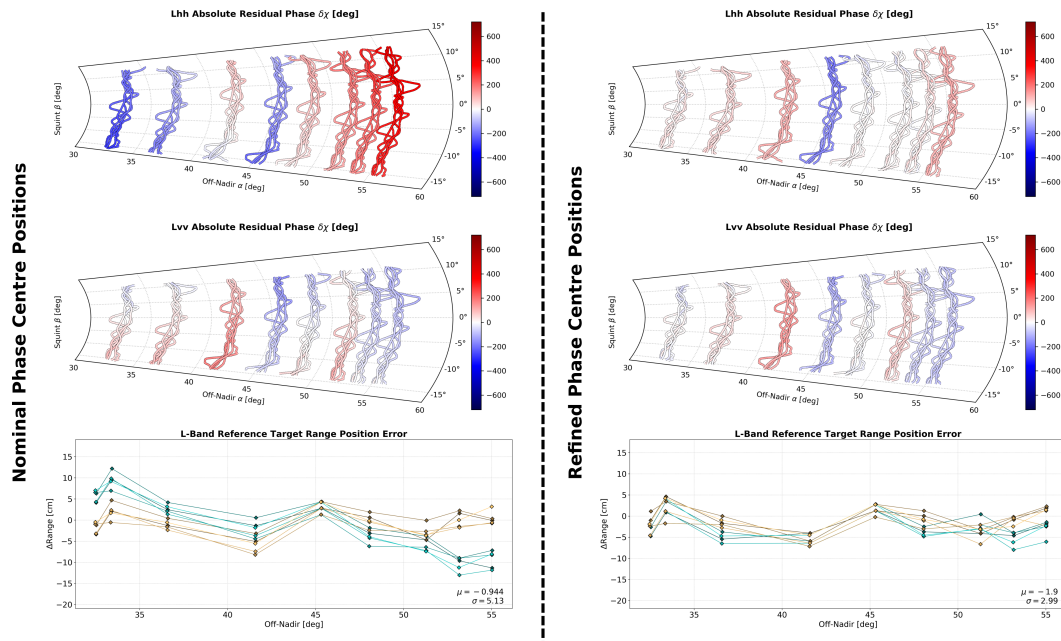


**Figure 12.** The impact of antenna element phase center position calibration on phase and position errors. The measurements shown are derived from the co-polar channels of five independent F-SAR calibration data acquisitions at L-band. The first and second row visualize the absolute residual phase  $\delta\chi_{pq}^s(az)$  derived from range compressed raw data in different polarizations, while the last row shows the reference target range position error as measured in focused SAR imagery. In the latter plots, each target is represented by a point and lines connect targets in the same channel (see the legend in Figure 13).

The top-left plot suggests that the measured range of reference targets in the HH channel is systematically biased: residual errors clearly show a trend across the sensor swath. This trend is confirmed by the corresponding target range position mismatch measured in focused SAR imagery, as illustrated by the turquoise lines in the bottom-left plot. A comparison of these results with those on the right side of the Figure shows that the estimated phase center position corrections  $\Delta\vec{L}_e$  effectively compensate for this trend. Not only does the correction make the measured target range positions more accurate, but the geometry of the two co-polarized channels has become highly consistent. This is the intended effect of the differential error term (32). The residual errors measured in focused SAR imagery after calibration, as shown in the bottom-right plot, are largely consistent with the uncertainties to be expected in the sensor navigation data and in the reference target phase center positions obtained via Differential GPS (DGPS).

While Figure 4 primarily shows the target range mismatch as a function of the off-nadir angle, range error variations do also occur as a function of squint. The top row of plots in Figure 13 emphasize

such variations by showing the residual  $\delta\chi_{pq}^s(az)$  after the mean value has been subtracted from each individual range history. The bottom row of plots, meanwhile, show the target azimuth position mismatch. The information in these plots is closely related: a linear phase error along the range history shifts the response in the focused image. As in the range dimension, phase center position calibration improves the overall geometric accuracy in azimuth. Simultaneously, it ensures consistent results across all polarization channels.

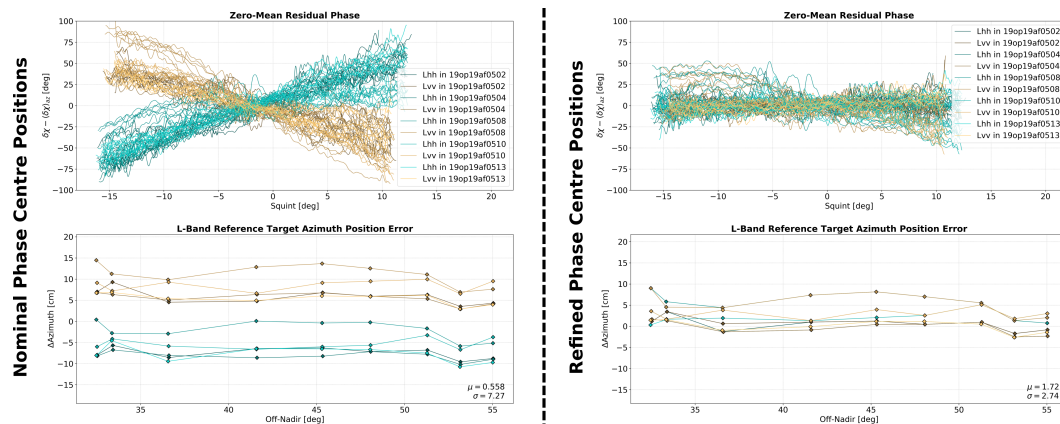


**Figure 13.** Similar to the analysis of Figure 12, but with an emphasis on the azimuth dimension. The top row shows the absolute residual phase  $\delta\chi_{pq}^s(az)$  variation as a function of the squint angle, after the mean phase has been subtracted from each response. The second row shows the reference target azimuth position error as measured in focused SAR imagery.

The results presented in this section indicate that the proposed phase center calibration model is able to improve the geometric fidelity of focused SAR imagery. It is not, however, possible to quantitatively evaluate the accuracy of the actual position estimates derived as the true phase center positions are simply not known. Qualitatively, however, the results appear plausible. The refined phase centers lie within one or two wavelengths distance from the geometric center of the physical antenna apertures. This holds true for all sixteen phase centers of the F-SAR antenna mount. To further confirm the robustness of the estimate, the L-band calibration detailed in this section was repeated several times. In each iteration, the initial phase center positions were randomly perturbed by  $\pm 1$  m in each dimension and the estimation process was repeated. The resulting phase center estimates were found to be in agreement with a standard deviation of under 2 mm.

A quantitative evaluation is even more difficult for the tropospheric propagation correction  $\Delta c$ , where optimization yields a value of  $6 \times 10^{-5}$  for the L-band results of this section. This correction changes the refractivity  $N_{air}$  from 283, the assumed default value, to 342 parts per million. Both of these values are plausible, in that they are reproducible by established models for reasonable choices of temperature, pressure and relative humidity [30]. While there has not been a systematic effort to validate this aspect of the calibration model further, phase center position corrections are generally smaller and appear more plausible when the tropospheric propagation correction is included in the underlying model. A rigorous analysis of this calibration parameter is, however, beyond the scope of the present discussion. To do so would require additional ground truth and simulations.

#### 5.4. Single-Pass Interferometry and Polarimetry

Interferometric and polarimetric applications, as well as DBF imaging, rely on phase consistency among data in several channels simultaneously acquired by the SAR sensor. This section presents results that illustrate how propagation direction independent phase consistency is achieved by the baseline calibration approach described in Section 4.4. The results in this section pertain to data acquired with the X-band polarimetric across track interferometer of F-SAR in 2014.

The impact of the baseline calibration process on the inter-channel phase differences of the interferometer is illustrated in Figure 14. The polar plots show phase differences between the range histories of reference targets deployed in the calibration site. The underlying raw data was acquired during the calibration campaign *OP14AF*. The evaluation covers all unique interferometric pairs among the co-polar channels acquired simultaneously by the interferometer. These are four channels corresponding to the two antennas, X1 and X2. The top and the bottom halves of the figure juxtapose interferometric phase errors before and after baseline calibration. The results clearly show that systematic trends are effectively removed from the two independent interferometric calibration data acquisitions considered. The evaluation shows that the errors addressed are, indeed, systematic across independent acquisitions and that the proposed baseline correction model is able to simultaneously explain residual errors in all possible channel combinations of a multi-channel SAR acquisition.

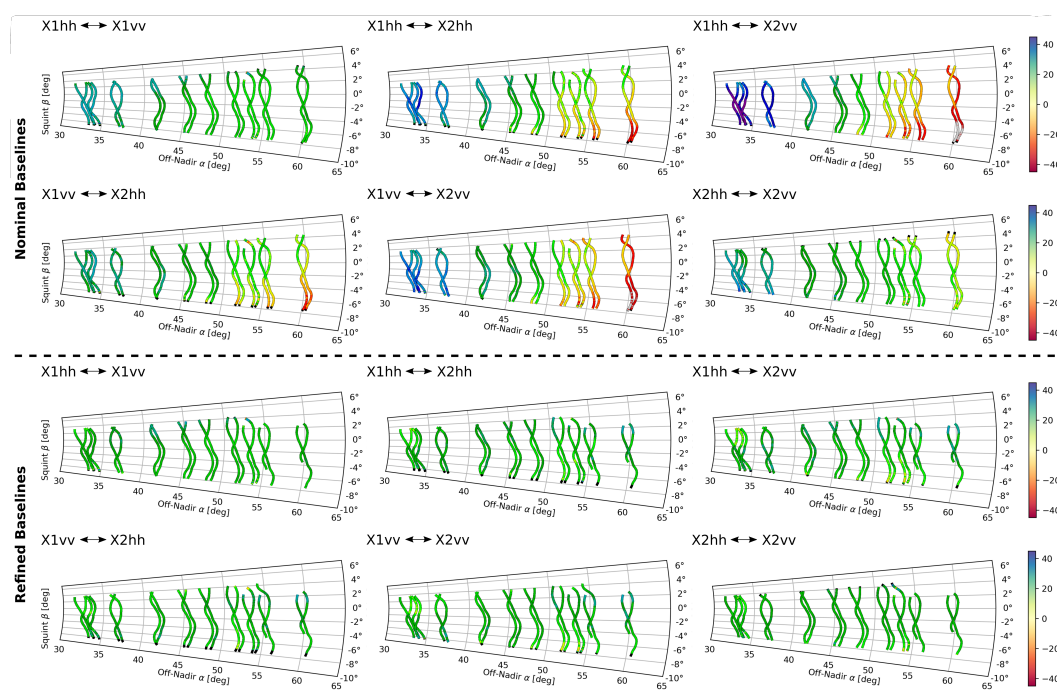


**Figure 14.** Residual interferometric phase errors along the range histories of reference targets in two independent polarimetric, interferometric X-band acquisitions. The top and the bottom halves of the figure show interferograms before and after baseline calibration, respectively. Each half comprises six plots that correspond to all possible combinations of four channels. The channels in this example are the four co-polar channels that are acquired, simultaneously, by the two polarimetric antennas in the F-SAR X-band across track interferometer.

Table 1 lists the position refinements corresponding to the results of Figure 14. Baseline calibration shifts the phase centers of the interferometer on the order of 1 mm. To further validate this correction, Figure 15 summarizes results obtained during the scientific measurement campaign *ICESAR*, which included acquisitions over the Rhone Glacier in Switzerland that were carried out days after the calibration acquisitions of *OP14AF* in September 2014. The results show how the baseline corrections of Table 1 significantly improve the consistency of digital surface models (DSMs) derived from F-SAR acquisitions with opposing look directions. The original DSM difference shown in the bottom left of Figure 15 is dominated by a clear trend. The result after calibration, on the other hand, appears to be free of systematic errors. Instead, it shows differences that may be of scientific interest: they could be related to variations in the penetration depth of the radar signal that depend on the local incidence angle.

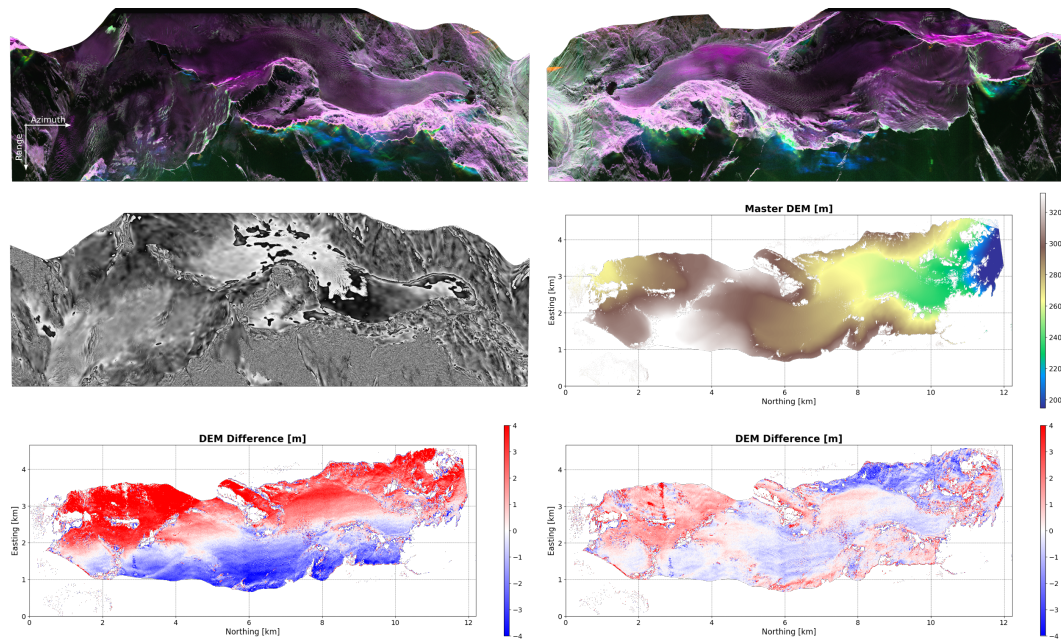


**Figure 15.** A comparison of the consistency of digital surface models (DSMs) extracted from F-SAR single pass interferometry over the Rhone glacier in Switzerland. **Top:** Polarimetric RGB color composites showing the backscatter amplitude in the lexicographic basis (HH, HV, VV) for two consecutive acquisitions with opposite look directions onto the glacier. **Middle:** The single-pass interferometric phase in the HH polarization, relative to the SRTM elevation model used for motion compensation, and the DSM derived therefrom. **Bottom:** The difference of the DSMs obtained, one for each look direction, assuming the nominal baseline (left) and using the refined baseline after calibration (right).

**Table 1.** The position refinements estimated for the four phase centers of the X-band polarimetric across track interferometer of F-SAR using the baseline optimization of Section 4.4. The changes are given in cm and correspond to those in the phase evaluation of Figure 14.

	Baselines [cm]		
	$\delta x$	$\delta y$	$\delta z$
X1h	0.121	0.065	0.051
X1v	0.014	−0.023	0.000
X2h	−0.041	−0.042	−0.050
X2v	−0.093	0.000	−0.001

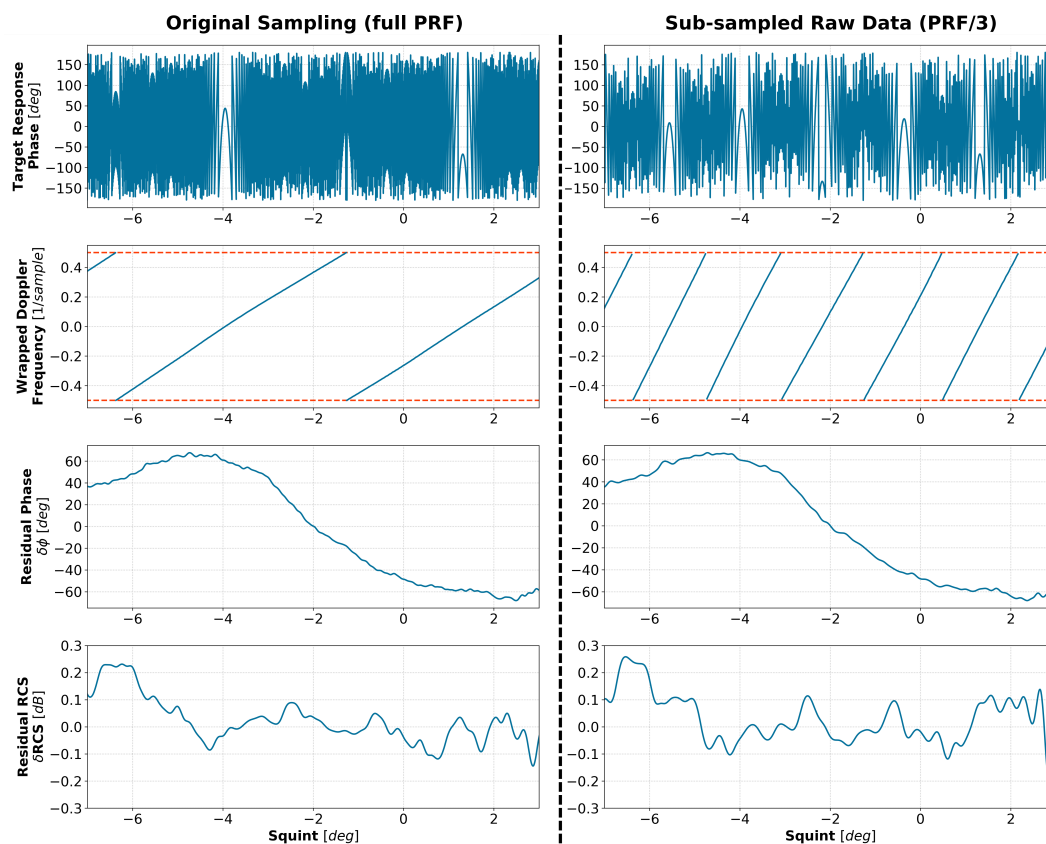
### 5.5. Calibration of Under-Sampled SAR Data

As the proposed calibration technique does not require azimuth compression, it does not require the azimuth sampling to fulfill the Nyquist criterion. As argued in Section 2, the latter point is of practical relevance in the context of DBF techniques, where independent channels are under-sampled but need to be interferometrically calibrated. Relevant examples of future spaceborne systems include HRWS systems with multiple azimuth apertures [31,32] but also multiple beam systems operating the SCORE concept to cover a larger swath [19].

Figure 16 illustrates, qualitatively, why sub-sampling is not an issue in the proposed approach. It compares the results of target analysis obtained for a single target at the full channel Pulse Repetition Frequency (PRF) and after the sampling rate has been artificially reduced by dropping two out of every three pulses of raw data. While the phase and frequency content of the raw data are, of course, severely affected by the sub-sampling, the inputs to the actual calibration process (the residual errors shown in



the bottom two rows) remain largely unaffected due to the compensation of the model phase (5) in the response correction of (8).



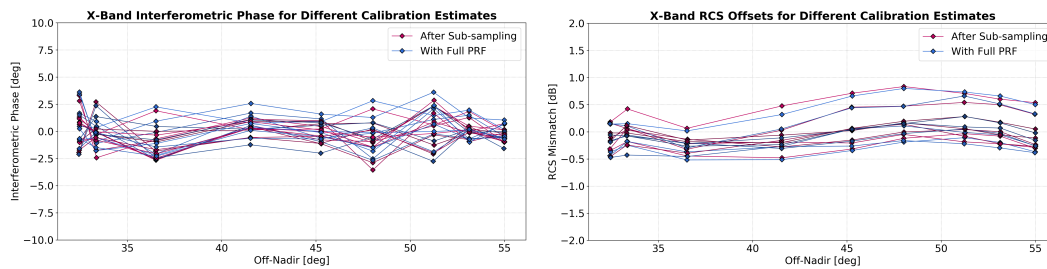
**Figure 16.** The impact of azimuth under-sampling on the residual errors obtained in the analysis of a trihedral reflector response at X-band. The left column summarizes the analysis of the original target response at the full azimuth sampling frequency. The right column shows the results obtained when only every third pulse of the raw data is used (the other pulses are discarded in pre-processing). The squint angle on the x-axis is defined in the antenna reference frame as in (6) and, for this particular response, the zero Doppler frequency corresponds to a squint of  $-4^\circ$ .

Table 2 quantifies the impact of sub-sampling on the calibration of the four X-band phase centers of the F-SAR across track interferometer. To derive these results, the sub-sampling of Figure 16 is applied to all raw data channels. The first three columns show the difference in the absolute phase center position. These differences amount to an offset of around 1 cm that has no measurable impact on the geometric accuracy of the data: constant range delays are absorbed by calibration constants, while the variation across the swath is negligible. The relative position changes, obtained by subtracting the mean from each of the first three columns. These are given in the middle columns and are on the order of 1 mm. The pointing changes, given in the last three columns, are significantly smaller than  $0.1^\circ$ . As illustrated in Figure 17, these baseline and pointing changes do not have a measurable impact on the observable calibration quality.



**Table 2.** The quantitative impact of severe azimuth under-sampling (see Figure 16) on the external calibration of the four phase centers comprising the polarimetric X-band across track interferometer of F-SAR. The columns of the table are as follows: *Positions* denote the change in phase center coordinates, *Baselines* are the same changes after the overall mean offset is subtracted, while *Antenna Pointing* denotes the changes in the antenna pointing angles.

	Positions [cm]			Baselines [cm]			Antenna Pointing [deg]		
	$\delta x$	$\delta y$	$\delta z$	$\delta x$	$\delta y$	$\delta z$	$\delta roll$	$\delta pitch$	$\delta yaw$
X1h	0.471	−0.108	0.952	0.000	0.061	0.065	0.007	0.026	−0.016
X1v	0.481	−0.214	0.840	0.010	−0.040	−0.047			
X2h	0.473	−0.173	0.884	0.001	−0.003	−0.003	0.002	0.045	−0.038
X2v	0.472	−0.164	0.894	0.001	0.005	0.006			



**Figure 17.** A comparison of the residual errors measured in two independent F-SAR X-band acquisitions. The plots juxtapose results after calibration with (red) and without (blue) sub-sampling the input data. The comparison is based on the raw data used for calibration and illustrates the impact of the baseline and pointing changes given in Table 2. Left: interferometric phase errors obtained in the six co-polar channel combinations of Figure 14. Each data point is obtained as an average over the illumination time of a reference target. Lines connect targets in the same interferometric channel combination. Right: the residual RCS mismatch in the four co-polar channels of the interferometer. As before, data points are obtained as an average over the target illumination time.

### 5.6. Limits of Applicability

This section briefly discusses the limits of the estimation algorithms presented in preceding sections. These limits are defined in terms of the magnitude of errors that can be corrected. They are summarized in Table 3.

**Table 3.** A summary of the limits of applicability of the proposed calibration procedure. Limits are quantified by the magnitude of the calibration corrections that can be reliably estimated. The left and right columns indicate the sensor parameter correction and the maximum permissible correction magnitude, respectively. The middle column indicates which of the residual errors in the target response are affected.

Parameter	Residuals affected	Max. Parameter Error
$\Delta \vec{A}_e$	$\delta \text{RCS}_{pq}^s(az)$	Antenna beam width
$\Delta \vec{L}_e$	$\delta \chi_{pq}^s(az), \delta \phi_{pq}^s(az)$	> 10 m at X-band
$\Delta c$	$\delta \chi_{pq}^s(az), \delta \phi_{pq}^s(az)$	> 2000 ppm at X-band

The maximum antenna pointing correction  $\Delta \vec{A}_e$  is roughly equal to the antenna beam width. It therefore depends on the frequency band and the antenna design. The results presented in Section 5.1, and Figure 10 in particular, demonstrate that the approach can correct for mispointing of a magnitude comparable to the azimuth beam width. This result, however, is close to the limit of what is possible for several reasons. Firstly, the linear approximation of Equation (29) eventually fails: assuming, for simplicity, that the antenna gain in the main beam is roughly quadratic, the 1st order Taylor

expansion implied in the approximation of (27) by (29) is only valid within the main beam (where the difference of two approximately quadratic functions is approximately linear). When this linear approximation fails, the fixed-point iteration for the pointing estimate will converge to meaningless results or may even diverge entirely. Secondly, very large pointing errors would make it difficult to even localize the reference target response in the raw data. Additional pre-processing steps might be required to bootstrap the calibration process.

In the case of the maximum phase center position correction  $\Delta\tilde{L}_e$ , simulations with artificially displaced phase centers suggest that errors of at least 10 m can be corrected: for the X-band data of Section 5.5, the corrected positions agree to within margins similar to those reported in Table 2. Even larger errors were not considered, as they appear of little practical relevance. Eventually, however, the calibration process would fail as the target response lies outside the range interval considered during analysis. Furthermore, these results are also the basis for the limit given for the tropospheric propagation correction  $\Delta c$ . The maximum correction given in the table, in parts per million, corresponds to a error in the range vector of  $\sim 10$  m for a typical altitude above ground of 5 km. This limit is far outside the range of variation encountered in nature [30].

Finally, another limiting factor to be considered in practice is the signal to noise ratio (SNR). The impact of noise may be an issue, as the proposed approach does not involve azimuth compression and therefore does not benefit from azimuth compression gain. The results of Section 5.5 are relevant in this regard: while they demonstrate that azimuth under-sampling does not present any fundamental difficulty in the calibration approach, under-sampling does ultimately have a detrimental impact on the accuracy attainable. Increasing under-sampling leads to increased clutter levels, even after clutter filtering, as more clutter contributions become aliased with the reference target response. This increase in clutter noise is evident in the plots of  $\delta\text{RCS}_{pq}^s(az)$  in the last row of Figure 16. The SNR is clearly not an issue for the sensor and acquisition geometries considered in the preceding sections. Should low SNR be a practical concern, however, the proposed calibration technique may yet remain applicable if either the PRF or the strength of the reference target radar return can be increased.

## 6. Conclusions

The paper introduces a new approach to the external calibration of multi-channel SAR sensors. A survey of results based on the analysis of multi-channel SAR data acquired by DLR's airborne F-SAR and DBFSAR sensors suggest that the approach can be used to effectively estimate calibration corrections to counteract propagation direction dependent effects, thereby significantly improving the radiometric and interferometric data calibration quality.

The calibration approach yields antenna phase center position and interferometric baseline corrections in three dimensions as well as three dimensional antenna pointing estimates. The results reported show that the antenna phase center refinement leads to improved and more consistent geometric accuracy in focused SAR imagery and also improves the fidelity of interferometric and polarimetric SAR phase measurements. The antenna pointing estimates, which are provided separately for transmit and receive where the multi-channel scenario demands it, are seen to improve the radiometric accuracy. Pointing corrections also compensate for systematic, residual amplitude variations in the Doppler spectrum after SAR processing.

Unlike current state of the art techniques, the method is based entirely on the analysis of range compressed raw data and does not require azimuth compression. It remains applicable in cases where azimuth compression presupposes accurate calibration and, in particular, can be applied to data that is irregularly or under-sampled in azimuth. This is especially relevant in view of the digital beam-forming techniques envisaged for future HRWS missions, such as the Tandem-L formation [33].

## 7. Patents

European Patent Number EP000003364212A1 ("*A method and an apparatus for computer-assisted processing of SAR raw data*"), published on 22 August 2018.

**Author Contributions:** Conceptualization, M.J.; Formal analysis, M.J.; Funding acquisition, A.R.; Investigation, M.J.; Methodology, M.J., R.S. and A.R.; Resources, R.S. and A.R.; Software, M.J.; Supervision, R.S.

**Funding:** This research received no external funding

**Conflicts of Interest:** The authors declare no conflict of interest.

## References

- Freeman, A. SAR calibration: An overview. *IEEE Trans. Geosci. Remote Sens.* **1992**, *30*, 1107–1121. [\[CrossRef\]](#)
- Werninghaus, R.; Buckreuss, S. The TerraSAR-X Mission and System Design. *IEEE Trans. Geosci. Remote Sens.* **2010**, *48*, 606–614. [\[CrossRef\]](#)
- Krieger, G.; Moreira, A.; Fiedler, H.; Hajnsek, I.; Werner, M.; Younis, M.; Zink, M. TanDEM-X: A Satellite Formation for High-Resolution SAR Interferometry. *IEEE Trans. Geosci. Remote Sens.* **2007**, *45*, 3317–3341. [\[CrossRef\]](#)
- Covello, F.; Battazza, F.; Coletta, A.; Lopinto, E.; Fiorentino, C.; Pietranera, L.; Valentini, G.; Zoffoli, S. COSMO-SkyMed an existing opportunity for observing the Earth. *J. Geodyn.* **2010**, *49*, 171–180. [\[CrossRef\]](#)
- Torres, R.; Snoeij, P.; Geudtner, D.; Bibby, D.; Davidson, M.; Attema, E.; Potin, P.; Rommen, B.; Floury, N.; Brown, M.; et al. GMES Sentinel-1 mission. *Remote Sens. Environ.* **2012**, *120*, 9–24. [\[CrossRef\]](#)
- Morena, L.C.; James, K.V.; Beck, J. An introduction to the RADARSAT-2 mission. *Can. J. Remote Sens.* **2004**, *30*, 221–234. [\[CrossRef\]](#)
- Reigber, A.; Scheiber, R.; Jager, M.; Prats-Iraola, P.; Hajnsek, I.; Jagdhuber, T.; Papathanassiou, K.P.; Nannini, M.; Aguilera, E.; Baumgartner, S.; et al. Very-High-Resolution Airborne Synthetic Aperture Radar Imaging: Signal Processing and Applications. *Proc. IEEE* **2013**, *101*, 759–783. [\[CrossRef\]](#)
- Reigber, A.; Jäger, M.; Fischer, J.; Horn, R.; Scheiber, R.; Prats, P.; Nottensteiner, A. System status and calibration of the F-SAR airborne SAR instrument. In Proceedings of the Geoscience and Remote Sensing Symposium (IGARSS), 2011 IEEE International, Vancouver, BC, Canada, 24–29 July 2011; pp. 1520–1523. [\[CrossRef\]](#)
- Bachmann, M.; Schwerdt, M.; Bräutigam, B. TerraSAR-X Antenna Calibration and Monitoring Based on a Precise Antenna Model. *IEEE Trans. Geosci. Remote Sens.* **2010**, *48*, 690–701. [\[CrossRef\]](#)
- Iorio, M.; Mecozzi, R.; Torre, A. Cosmo SkyMed: Antenna elevation pattern data evaluation. *Ital. J. Remote Sens.* **2010**, *42*, 69–77. [\[CrossRef\]](#)
- Schwerdt, M.; Schmidt, K.; Ramon, N.T.; Alfonzo, G.C.; Döring, B.J.; Zink, M.; Prats-Iraola, P. Independent verification of the Sentinel-1A system calibration. *IEEE J. Sel. Top. Appl. Earth Obs. Remote Sens.* **2016**, *9*, 994–1007. [\[CrossRef\]](#)
- Calabrese, D.; Cricenti, A.; Grimani, V.; Scaranari, D.; Vigliotti, R.; Covello, F.; Marano, G. COSMO-SkyMed: Calibration & validation resources and activities. In Proceedings of the 2008 IEEE Radar Conference, Rome, Italy, 26–30 May 2008; pp. 1–6.
- Luscombe, A.P. RADARSAT-2 SAR image quality and calibration operations. *Can. J. Remote Sens.* **2004**, *30*, 345–354. [\[CrossRef\]](#)
- Jirousek, M.; Döring, B.; Rudolf, D.; Raab, S.; Schwerdt, M. Development of the highly accurate DLR Kalibri transponder. In Proceedings of the EUSAR 2014; 10th European Conference on Synthetic Aperture Radar, Berlin, Germany, 3–5 June 2014; pp. 1–4.
- Touzi, R.; Hawkins, R.K.; Cote, S. High-Precision Assessment and Calibration of Polarimetric RADARSAT-2 SAR Using Transponder Measurements. *IEEE Trans. Geosci. Remote Sens.* **2013**, *51*, 487–503. [\[CrossRef\]](#)
- Ulander, L. Accuracy of using point targets for SAR calibration. *IEEE Trans. Aerosp. Electron. Syst.* **1991**, *27*, 139–148. [\[CrossRef\]](#)
- Bickel, D.; Hensley, W. Interferometric SAR phase difference calibration: Methods and results. In Proceedings of IGARSS '94-1994 IEEE International Geoscience and Remote Sensing Symposium, Pasadena, CA, USA, 8–12 August 1994; Volume 4, pp. 2259–2262.
- Ponce, O.; Prats-Iraola, P.; Pinheiro, M.; Rodriguez-Cassola, M.; Scheiber, R.; Reigber, A.; Moreira, A. Fully-Polarimetric High-Resolution 3-D Imaging with Circular SAR at L-Band. *IEEE Trans. Geosci. Remote Sens.* **2014**, *52*, 3074–3090. [\[CrossRef\]](#)
- Villano, M.; Krieger, G.; Moreira, A. Staggered SAR: High-resolution wide-swath imaging by continuous PRI variation. *IEEE Trans. Geosci. Remote Sens.* **2013**, *52*, 4462–4479. [\[CrossRef\]](#)

20. Prats-Iraola, P.; Scheiber, R.; Rodriguez-Cassola, M.; Mittermayer, J.; Wollstadt, S.; De Zan, F.; Bräutigam, B.; Schwerdt, M.; Reigber, A.; Moreira, A. On the Processing of Very High Resolution Spaceborne SAR Data. *IEEE Trans. Geosci. Remote Sens.* **2014**, *52*, 6003–6016. [[CrossRef](#)]
21. Curlander, J.; McDonough, R. *Synthetic Aperture Radar: Systems and Signal Processing*; Wiley Series in Remote Sensing and Image Processing; Wiley: New York, NY, USA, 1991.
22. Gabler, B.; Kosc, A.; Limbach, M. Antenna Range Measurements for Airborne Remote Sensing Antennas. In Proceedings of the European Conference on Antennas and Propagation (EuCAP), London, UK, 9–14 April 2018.
23. Ruck, G. *Radar Cross Section Handbook*; Plenum Press: New York, NY, USA, 1970.
24. Scheiber, R.; Moreira, A. Coregistration of interferometric SAR images using spectral diversity. *IEEE Trans. Geosci. Remote Sens.* **2000**, *38*, 2179–2191. [[CrossRef](#)]
25. Boyd, S.; Boyd, S.; Vandenberghe, L.; Press, C.U. *Convex Optimization*; Berichte über Verteilte Messsysteme; Cambridge University Press: Cambridge, UK, 2004.
26. Quegan, S.; Lamont, J. Ionospheric and tropospheric effects on synthetic aperture radar performance. *Int. J. Remote Sens.* **1986**, *7*, 525–539. [[CrossRef](#)]
27. Shanker, A.P.; Zebker, H.A. Sparse Two-Dimensional Phase Unwrapping Using Regular Grid Methods. *IEEE Geosci. Remote Sens. Lett.* **2009**, *6*, 519–522. [[CrossRef](#)]
28. Bioucas-Dias, J.M.; Valadao, G. Phase unwrapping via graph cuts. *IEEE Trans. Image Process.* **2007**, *16*, 698–709. [[CrossRef](#)]
29. Reigber, A.; Nottensteiner, A.; Limbach, M.; Jäger, M.; Kosc, A.; Scheiber, R.; Fischer, J.; Catalan, D.L.; Müller, G.; Künemund, M.; et al. First Interferometric Trials with the Airborne Digital-Beamforming DBFSAR System. In Proceedings of the European Conference on Synthetic Aperture Radar (EUSAR), Aachen, Germany, 4–7 June 2018; pp. 12–15.
30. Fabry, F.; Frush, C.; Zawadzki, I.; Kilambi, A. On the extraction of near-surface index of refraction using radar phase measurements from ground targets. *J. Atmos. Ocean. Technol.* **1997**, *14*, 978–987. [[CrossRef](#)]
31. Krieger, G.; Younis, M.; Gebert, N.; Huber, S.; Bordoni, F.; Patyuchenko, A.; Moreira, A. Advanced Concepts for High-Resolution Wide-Swath SAR Imaging. In Proceedings of the European Conference on Synthetic Aperture Radar (EUSAR), Aachen, Germany, 7–10 June 2010; pp. 524–527.
32. Gebert, N.; Krieger, G.; Moreira, A. Digital Beamforming on Receive: Techniques and Optimization Strategies for High-Resolution Wide-Swath SAR Imaging. *IEEE Trans. Aerosp. Electron. Syst.* **2009**, *45*, 564–592. [[CrossRef](#)]
33. Moreira, A.; Krieger, G.; Hajnsek, I.; Papathanassiou, K.; Younis, M.; Lopez-Dekker, P.; Huber, S.; Villano, M.; Pardini, M.; Eineder, M.; et al. Tandem-L: A highly innovative bistatic SAR mission for global observation of dynamic processes on the Earth's surface. *IEEE Geosci. Remote Sens. Mag.* **2015**, *3*, 8–23. [[CrossRef](#)]

